

# Interactions of jets with inhomogeneous cloudy media

Curtis J. Saxton,<sup>1,2,3★</sup> Geoffrey V. Bicknell,<sup>3,4★</sup> Ralph S. Sutherland<sup>3★</sup>  
and Stuart Midgley<sup>5★</sup>

<sup>1</sup>*Mullard Space Science Laboratory, University College London, Holmbury St Mary, Dorking, Surrey RH5 6NT*

<sup>2</sup>*Max-Planck-Institut für Radioastronomie, Auf dem Hügel 69, D-53121 Bonn, Germany*

<sup>3</sup>*Research School of Astronomy & Astrophysics, Mt Stromlo Observatory, Australian National University, Weston ACT 2611, Australia*

<sup>4</sup>*Department of Physics & Theoretical Physics, Faculty of Science, Australian National University ACT 0200, Australia*

<sup>5</sup>*ANU Supercomputer Facility, Australian National University ACT 0200, Australia*

Accepted 2005 February 22. Received 2005 February 22; in original form 2004 November 22

## ABSTRACT

We present two-dimensional slab-jet simulations of jets in inhomogeneous media consisting of a tenuous hot medium populated with a small filling factor by warm, dense clouds. The simulations are relevant to the structure and dynamics of sources such as gigahertz peak spectrum and compact steep spectrum (CSS) radio galaxies, high-redshift radio galaxies and radio galaxies in cooling flows. The jets are disrupted to a degree depending upon the filling factor of the clouds. With a small filling factor, the jet retains some forward momentum but also forms a halo or bubble around the source. At larger filling factors channels are formed in the cloud distribution through which the jet plasma flows and a hierarchical structure consisting of nested lobes and an outer enclosing bubble results. We suggest that the CSS quasar 3C 48 is an example of a low filling factor jet–interstellar medium interaction while M87 may be an example of the higher filling factor type of interaction. Jet disruption occurs primarily as a result of Kelvin–Helmholtz instabilities driven by turbulence in the radio cocoon not through direct jet–cloud interactions, although there are some examples of these. In all radio galaxies whose morphology may be the result of jet interactions with an inhomogeneous interstellar medium we expect that the dense clouds will be optically observable as a result of radiative shocks driven by the pressure of the radio cocoon. We also expect that the radio galaxies will possess faint haloes of radio-emitting material well beyond the observable jet structure.

**Key words:** hydrodynamics – ISM: clouds – galaxies: active – galaxies: individual: 3C 48 – galaxies: ISM – galaxies: jets.

## 1 INTRODUCTION

Previous models of jets propagating through the interstellar medium of radio galaxies have almost always assumed a uniform, usually hot ( $T \sim 10^7$  K) interstellar medium. These models have contributed substantially to our understanding of the propagation of jets in evolved radio galaxies wherein much of the dense matter that could have previously obstructed the jets has been cleared away. However, it is now clear that in many young radio galaxies, i.e. gigahertz peak spectrum (GPS) and compact steep spectrum (CSS) sources, substantial interaction between the expanding radio plasma and dense interstellar clouds occurs. This interaction has a number of effects. Two of the most important are that it significantly distorts the radio morphology and it also gives rise to shock-excited

line emission. Strong observational evidence for the latter effect has been obtained from combined *Hubble Space Telescope* (*HST*) and radio observations of a number of CSS sources (de Vries et al. 1999; Labiano et al. 2003; O’Dea et al. 2003) showing a strong alignment effect between optical and radio emission and clear evidence for disturbance of the optically emitting gas by the expanding radio lobe. On the other hand, the dense gas cannot have a large filling factor in the case of GPS and CSS sources since the expansion speed of the radio plasma is usually quite high:  $\sim 0.1$ – $0.4 c$  (Murgia et al. 1999; Parma et al. 1999; Conway 2002a; Murgia et al. 2002; Murgia 2003). Thus the picture that is conveyed by the combined radio and optical observations is of radio plasma propagating through a predominantly hot and tenuous interstellar medium in which dense clouds are embedded with a low filling factor. Nevertheless, as we show in this paper, even a low filling factor of dense gas can have a pronounced effect on the evolution of the radio lobes.

High-redshift radio galaxies provide another example in which radio plasma–cloud interactions are clearly important. For example,

\*E-mail: cjs2@mssl.ucl.ac.uk (CJS); geoff@mso.anu.edu.au (GVB); ralph@mso.anu.edu.au (RSS); Stuart.Midgley@anu.edu.au (SM)

in the high-redshift radio galaxy 4C 41.17, interactions between the jets and large clouds in the Lyman- $\alpha$  emitting halo of the parent galaxy lead to shock-excited line emission and to accelerated rates of star formation (Bicknell et al. 1998). Returning to the low-redshift Universe, radio plasma-clumpy ISM interactions may be responsible for the heating of the ISM that is necessary to counteract the otherwise large mass inflow rates that are inferred from X-ray observations of cooling flows.

Thus, there is ample physical motivation for detailed investigations of the manner in which jets and the related radio lobes interact with realistic interstellar media. One of the most significant drivers of this research is that all of the scenarios discussed above represent examples of active galactic nucleus (AGN)–galaxy feedback which, it has been argued (e.g. Silk & Rees 1998; Kawakatu, Umemura & Mori 2003), is a significant determinant of the ultimate structure of galaxies and in particular, the relation between the mass of the central black hole and the mass of the galaxy bulge (Magorrian et al. 1998; Tremaine et al. 2002).

In this first paper in this series we explore the nature of the interaction between jets and their lobes through a series of two-dimensional slab-jet simulations. The advantage of this approach is that two-dimensional simulations offer the prospect of high resolution and an initial rapid investigation of parameter space, which capture some of the features of more realistic three-dimensional simulations. Fully three-dimensional simulations will be presented in future papers.

The choice of coordinate system is non-trivial when representing supersonic jets in two spatial dimensions. Many aspects of a jet burrowing through a uniform external medium have been adequately described in the past by axisymmetric simulations. However, an axisymmetric simulation is less appropriate for physical systems where the jet is expected to be bent or deflected. When colliding directly with a dense cloud, an axisymmetric jet must either burrow through the cloud or cease its advance. However, a two-dimensional slab-jet can be deflected, although both jet and cloud are essentially infinite in the direction perpendicular to the computational grid. Our present work is concerned with systems where jet–cloud collisions and indirect interactions dominate. We therefore opt for a Cartesian grid and simulate transient slab-jets.

## 2 CHOICE OF JET AND ISM PARAMETERS

### 2.1 Jet energy flux, cloud and ISM density

The choice of jet parameters is based on a self-similar model for lobe expansion (Bicknell, Dopita & O’Dea 1997, based upon the model by Begelman 1996). In this model, the lobe is driven by a relativistic jet which expands in such a way that  $\zeta$ , the ratio of hot spot to lobe pressure, is constant. A value  $\zeta \sim 2$  was inferred by Begelman from simulations by Lind et al. (1989). Let  $\rho_0$  be the atmospheric mass density at a fiducial distance  $R_0$  from the core, let  $\delta$  be the index of the power variation of atmospheric density with radius [ $\rho = \rho_0 (R/R_0)^{-\delta}$ ] and let the jet energy flux be  $F_E$ . The temperature of the external medium is unimportant in this model since it is the inertia of the background medium that governs the expansion of the lobe. The advance speed,  $v_b$  of the head of the bow-shock as a function of distance  $R$  from the core is given by:

$$\begin{aligned} \frac{v_b}{c} &= \frac{3}{[18(8-\delta)\pi]^{1/3}} \zeta^{1/6} \left( \frac{F_E}{\rho_0 R_0^2} \right)^{1/3} \left( \frac{R}{R_0} \right)^{(\delta-2)/3} \\ &\approx 0.073 \left( \frac{F_{E,46}}{n(100 \text{ pc})} \right)^{1/3} \left( \frac{R}{100 \text{ pc}} \right)^{-1/6} \end{aligned} \quad (1)$$

where the jet energy flux is  $10^{46} F_{E,46} \text{ erg s}^{-1}$ ,  $n(100 \text{ pc})$  is the number density at 100 pc and the numerical values are for  $\zeta = 2$  and  $\delta = 1.5$ . Typical expansion speeds of CSS and GPS sources are of order  $(0.05\text{--}0.4)c$  with the largest velocities measured for the most compact sources (Murgia et al. 1999; Conway 2002a). Conway (2002b) has reviewed estimates of number densities  $\sim 1 \text{ cm}^{-3}$  for three GPS sources, and so a fiducial value of  $n(100 \text{ pc}) = 1 \text{ cm}^{-3}$  is reasonable. Compatibility of the expansion speeds estimated from equation (1) and the observations indicates jet energy fluxes in the range of  $10^{46\text{--}47} \text{ erg s}^{-1}$ . Jets of this power are also consistent with a conventional ratio  $\sim 10^{12\text{--}10^{11}} \text{ Hz}^{-1}$  of 1.4-GHz monochromatic radio power to jet energy flux and a median power at 5 GHz  $\sim 10^{27.5} \text{ W Hz}^{-1}$ . Nevertheless, in other sources which morphologically resemble CSS radio galaxies, such as the less radio powerful luminous infrared galaxies studied by Drake et al. (2003), it is apparent that the jet powers are somewhat less. Thus, in our simulations, we have adopted jet powers of  $10^{45}$  and  $10^{46} \text{ erg s}^{-1}$ .

*Hubble Space Telescope* observations (de Vries et al. 1997, 1999; O’Dea et al. 2002) show abundant evidence for dense clouds of emission-line gas associated with CSS radio galaxies and quasars. For a temperature  $10^4 T_{c,4} \text{ K}$  of the dense clouds, a number density  $n_x \sim 1 \text{ cm}^{-3}$  and temperature  $10^7 T_{x,7} \text{ K}$  for the hot interstellar medium, the number density in the clouds is  $n_c \approx 10^3 n_x T_{x,7}/T_{c,4} \text{ cm}^{-3}$ , assuming that the initial, undisturbed clouds are in pressure equilibrium with their surroundings. If we adopt such a value for the density of the interstellar medium then equation (1) implies that the velocity of advance would be  $\sim 0.02 c$  – much lower than what is observed. Hence, as discussed in Section 1, the dense clouds must have a small filling factor. Accordingly, in the simulations described below, we create clouds of approximately the inferred density and investigate the effect of various filling factors.

With the inferred radio source and cloud geometry, the line emission originates from dense, relatively cool clouds that are shocked as they are overrun by the expanding radio source. A model of this type was proposed by de Vries et al. (1999) and elaborated by Bicknell, Saxton & Sutherland (2003). In both treatments, the excess pressure of the advancing radio lobe drives shocks into the dense clouds. In the simulations described below, this is seen to occur but some direct jet–cloud collisions are also apparent. For radio lobe driven shocks (the main source of shocks), the shock velocity is:

$$v_{\text{sh}} \approx 950 \left( \frac{v_b}{0.1 c} \right) \left( \frac{n_c/n_x}{10^3} \right)^{1/2} \text{ km s}^{-1} \quad (2)$$

where  $n_c$  and  $n_x$  are the cloud and ISM number densities, respectively. Shocks in the velocity range  $300\text{--}950 \text{ km s}^{-1}$  are produced for bow-shock advance speeds  $\sim 0.1 c$  and density ratios  $n_c/n_x \sim 10^4\text{--}10^3$ . This is in accord with the observed velocity dispersions and velocity offsets inferred from *HST* spectra of a sample of CSS sources (O’Dea et al. 2002).

Radiative shocks do not develop instantaneously; the time required for a shock to become fully radiative is effectively the time,  $t_4$ , required for post-shock gas to cool to  $\sim 10^4 \text{ K}$ . In order that there be a display of optical emission lines,  $t_4$  must be less than a fraction  $f \sim 1$  of the dynamical time associated with the expansion of the lobe. In estimating  $t_4$  we utilize a cooling function, which estimates the non-equilibrium cooling following a high-velocity shock, and which is derived from the results of the one-dimensional MAPPINGS III code (Sutherland & Dopita 1993). This cooling function is also used in our simulations described below. The condition on  $t_4$  becomes a

condition on the bow-shock velocity

$$\left(\frac{v_b}{c}\right) < 0.07 f^{0.2} \left(\frac{n_c}{10^4 \text{ cm}^{-3}}\right)^{0.2} \times \left(\frac{n_c/n_x}{10^4}\right)^{0.4} \left(\frac{R}{\text{kpc}}\right)^{0.2} \quad (3)$$

(Bicknell et al. 2003). This upper limit on  $v_b$  is insensitive to the various parameters, in particular,  $f$ . If condition (3) is not satisfied near the head of the radio lobe it may be satisfied at the sides where the bow-shock expansion speed is about a factor of 2 lower. In this case one would expect to see emission from the sides but not the apex of the radio source. This condition gives a limiting bow-shock velocity  $v_b \sim 0.1 c$ . Therefore, it would be interesting to see whether the more rapidly expanding sources have a lower ratio of emission-line flux to radio power, and whether the emission-line flux is distributed in a different manner to that in lower velocity sources. These conditions may also be related to the causes of the trailing optical emission in CSS sources (de Vries et al. 1999). There are two possibilities: (a) the apex of the bow-shock is non-radiative (if  $v_b$  exceeds the above limit) or (b) the number of dense clouds per unit volume decreases at a few kpc from the core, i.e. beyond the normal extent of the narrow-line region. We are inclined to favour option (b) but (a) should also be kept in mind.

The simulations capture these characteristics that depend on the time of the effective onset of radiative shocks in the clouds. We see a range of shock conditions varying from almost pure adiabatic shocks to strongly radiative. When the cooling time of gas becomes shorter than the Courant time for the simulation, the integration of the energy equation ensures that the radiative shock occupies approximately one pixel in which the gas temperature is equal to the predefined equilibrium temperature ( $10^4$  K in these simulations).

## 2.2 Overpressured jets – Mach number and density ratio

In order to carry out realistic 2D simulations, we wish to establish jets with powers per unit transverse length that are relevant to the types of radio galaxies mentioned in the introduction, in combination with other reasonable values of parameters such as jet width and density. If the number density of the interstellar medium is  $\sim 1 \text{ cm}^{-3}$  on 100 pc scales, then the jet must be overpressured. We first show this in the context of a subrelativistic jet model and then support the proposition with a relativistic jet model.

Let a non-relativistic jet have a density  $\eta$  times that of the external medium, an internal Mach number  $M$ , a specific heat ratio  $\gamma$ , a pressure  $\xi$  times the external ISM pressure and a cross-sectional area  $A_j$ . Further, let  $\rho_x$  and  $v_x$  be the density and isothermal sound speed of the ISM. Then the jet mass, momentum and energy fluxes are, collecting the dimensional quantities on the left,

$$\dot{M} = (\rho_x v_x A_j) M \sqrt{\gamma \xi \eta} \quad (4)$$

$$\Pi = (\rho_x v_x^2 A_j) \xi (1 + \gamma M^2) \quad (5)$$

$$F_E = (\rho_x v_x^3 A_j) M \left( \frac{1}{\gamma - 1} + M^2 \right) \sqrt{\frac{\gamma^3 \xi^3}{\eta}} \quad (6)$$

Equation (6) clearly shows that the energy flux can be made arbitrarily large by decreasing the density ratio  $\eta$ . However, there is a natural lower limit on  $\eta$  – the value at which an initially relativistic jet becomes transonic. The critical value is defined by the condition  $\rho_j c^2 / 4 p_j = 1$  (Bicknell 1994), implying that  $\eta_{\text{crit}} = 4 \xi (v_x/c)^2 \approx$

$5.9 \times 10^{-6} \xi T_{x,7}$ . With the overpressure factor,  $\xi = 1$ ,  $\eta = 10^{-5}$ , a jet diameter of 10 pc,  $T_x = 10^7$  K and  $M = 20$ , the energy flux is only  $\sim 10^{44} \text{ erg s}^{-1}$ . One requires an overpressure factor of about 100 to achieve  $10^{46} \text{ erg s}^{-1}$ .

This result is easily verified for a relativistic jet whose energy flux is given by

$$F_E = (\rho_x v_x^2 c A_j) 4 \xi \beta_{\text{jet}} \Gamma_{\text{jet}}^2 \left[ 1 + \frac{\Gamma_{\text{jet}} - 1}{\Gamma_{\text{jet}}} \chi \right] \quad (7)$$

where  $\chi = \rho_j c^2 / 4 p_j$ , and  $\rho_j$  and  $p_j$  are the jet rest-mass density and pressure, respectively. If  $\xi = 1$ ,  $\Gamma = 10$ , a jet diameter of 10 pc,  $T_x = 10^7$  K and  $\chi = 0$  (the latter being appropriate for a jet dominated by relativistic plasma), then the energy flux is only  $1.2 \times 10^{43} \text{ erg s}^{-1}$ . Hence, for a relativistic jet, we require  $\xi \sim 10^{2-3}$  in order to achieve the required jet power. This conclusion would change if the jet energy density were dominated by cold matter, although this is generally not assumed to be the case.

Is an overpressured jet physical? The overpressure ratio refers to the pressure with respect to the undisturbed interstellar medium. However, the lobe itself is overpressured as a result of the advancing bow-shock so that it is possible for the jet to be in approximate equilibrium with the ambient lobe. In a real galaxy the overpressured lobe may not extend back to the core, in which case an overpressured jet would behave initially like a classical overpressured, underexpanded jet.

Therefore, in our simulations, we have adopted low values of the density ratio,  $\eta \sim 10^{-3}$ , Mach numbers,  $M$ , of the order of 10 and a high overpressure ratio in order to obtain the necessarily high jet energy fluxes (or their equivalent in 2D). Such a low value of  $\eta$  has the additional effect of producing superluminal velocities ( $\beta \sim 5-6$ ) in some simulations, highlighting the shortcomings of simulating powerful jets with a non-relativistic code. However, the essential point is that it is mainly the jet power that is physically important in jet–cloud interactions.

One could adopt the strategy of adopting non-relativistic parameters that correspond more closely to those of relativistic jets, for example by equating the velocity and pressure and matching either the power or thrust (e.g. see Komissarov & Falle 1996; Rosen et al. 1999). We have not done this explicitly here since there is no transformation that perfectly maps a non-relativistic flow into a relativistic equivalent. Clearly, this initial investigation of parameter space needs to be followed by more comprehensive simulations utilizing a fully relativistic code.

## 2.3 Prescription for cloud generation

In our simulations we prescribe a uniform density for the hot interstellar medium. Within this medium we establish an initial field of dense clouds that mimics the distribution of clouds in the interstellar medium, with a random distribution of positions, shapes and internal density structures. We consider that this is more desirable than specifying, say, circular clouds, albeit with random centres; in that case the subsequent evolution may be governed by the initial symmetry. An advantage of the approach that we describe here is that the distribution of the sizes, shapes and directions of propagation of radiative shocks is more realistic than that obtained from initially highly symmetric clouds.

We prescribe the density and distribution of clouds using a Fourier approach. In the first step we establish a grid of complex numbers in Fourier space and assign a random phase to each point. The largest wavenumber is compatible with the spatial resolution of the simulations. An amplitude filter is applied,  $\propto |\mathbf{k}|^{-5/3}$ , in order to mimic

**Table 1.** Parameters and properties of the intercloud medium and initial cloud fields in the respective simulations. The X-ray-emitting intercloud medium has temperature  $T_x$  and particle number density  $n_x$ . Clouds have a minimum density  $n_{c,\min}$ , mean density  $\bar{n}_c$ . The cloud generation threshold is  $\sigma_{\min}$  and the clouds occupy a total area  $A_c$ , corresponding to a filling factor of  $f_c$ . The total exposed cloud perimeter is  $P_c$ .

Model	$T_x$ (K)	$n_x$ ( $\text{cm}^{-3}$ )	$n_{c,\min}/n_x$	$\bar{n}_c/n_x$	$\sigma_{\min}$	$A_c$ ( $\text{pc}^2$ )	$f_c$	$P_c$ (pc)
A1	$10^7$	$10^{-2}$	300	500	1.9	$7.28 \times 10^5$	$2.92 \times 10^{-2}$	$5.83 \times 10^4$
B1	$10^7$	1	500	1000	2.6	$1.55 \times 10^3$	$4.11 \times 10^{-3}$	$6.16 \times 10^2$
B2	$10^7$	1	500	1000	1.9	$1.15 \times 10^4$	$3.04 \times 10^{-2}$	$3.51 \times 10^3$
B3	$10^7$	1	500	1000	1.2	$4.43 \times 10^4$	$1.18 \times 10^{-1}$	$9.74 \times 10^4$
B3a	$10^7$	1	500	1000	1.2	$4.43 \times 10^4$	$1.18 \times 10^{-1}$	$9.74 \times 10^4$

the power spectrum of structures formed by turbulence. Taking the Fourier transform of the wavenumber data produces an array of density fluctuations in real space. These fluctuations,  $\sigma(\mathbf{r})$ , are normalized so that their mean is 0 and their variance is 1. The final number density of gas is then defined by the relation:

$$n = \begin{cases} n_{\min} + n_{\sigma}(\sigma - \sigma_{\min}) & \text{wherever } \sigma \geq \sigma_{\min} \\ n_x & \text{elsewhere,} \end{cases} \quad (8)$$

where  $n_x$  is the number density of hot intercloud gas,  $n_{\min}$  is the minimum number density of gas in a dense cloud,  $n_{\sigma}$  is a scaling factor and  $\sigma_{\min}$  is a threshold value determining whether a particular cell is part of a cloud or else hot intercloud medium. In practice we choose the mean density of cloud gas,  $\bar{n}$ , and set the value of  $n_{\sigma}$  implicitly.

We apply upper and lower limits to the density distribution in  $k$ -space. Amplitudes are zeroed for  $k < k_{\min}$ , where  $k_{\min}$  corresponds to the Jeans wavenumber. This prevents the insertion of clouds that would have collapsed to form stars and also avoids the generation of a cloud field dominated by a single large cloud-mass. Amplitudes are also zeroed for  $k > k_{\max}$  where  $k_{\max}$  corresponds to 3 or 4 pixels of spatial resolution. Fine features, at the 3–4 pixel level, can introduce excessive and artificial sensitivity to effects on the level of individual pixels.

Finally, radial limits are applied to the cloud field as a whole. An outer limit,  $r_{\max}$  (typically  $\sim 0.5$ – $5$  kpc), limits the extent of the cloud field. The inner radius,  $r_{\min}$ , is defined by the Roche limit in the vicinity of a black hole:

$$r_{\min} = \left( \frac{3}{4\pi} \frac{M_{\text{bh}}}{\rho_c} \right)^{1/3}. \quad (9)$$

If the black hole mass is  $M_{\text{bh}} = 10^9 M_{\odot}$  and the cloud density is  $\rho_c \approx 15 M_{\odot} \text{pc}^{-3}$  then  $r_{\min} \approx 250$  pc.

Table 1 presents a summary of the properties of the clouds and intercloud medium, and the extent of cloud coverage in our simulations (which are each described in specific detail in Section 3). Figs 1 and 2 represent the initial distributions of cloud and intercloud gas in three of our simulations. Figs 3 and 4 show how the masses of individual clouds are distributed in the initial conditions of four of our simulations. As the cumulative distribution functions show, most clouds have masses of less than a few thousand solar masses. The scatter plots show the characteristic depth of clouds: in mean terms the distance from an interior point to the surface is  $r = DI/S$ , where  $D$  is the number of spatial dimensions,  $I$  is the interior (area of a 2D cloud) and  $S$  is the surface (perimeter of a 2D cloud). A small  $r$  means that most of the cloud mass is well exposed to surface effects, such as ablation and the penetration of shocks from outside. If  $r$  is large than the interior regions are typically deeper from the

locally nearest surface, and correspondingly better insulated from effects at the surface.

Large clouds, near the Jeans limit (e.g. thickness  $2r \sim 105$  pc in the B series), are rare in every simulation. The simulations with a greater cut-off,  $\sigma_{\min}$ , and hence greater filling factor of clouds, also feature individual clouds of greater mass than the simulations with lower  $\sigma_{\min}$ .

## 2.4 Code

In the simulations reported here, we have used a locally modified version of a Piecewise Parabolic Method (Colella & Woodward 1984) code, known as VH-1, published on the Web by the computational astrophysics groups at the Universities of Virginia and South Carolina.<sup>1</sup> Our modifications of the VH-1 code include restructuring of the code for efficient computation on the computers at the Australian National University (formerly a Fujitsu VP300; now a Compaq Alphaserver SC), addition of code for dynamically important cooling and other code for coping with a numerical shock instability (Sutherland, Bisset & Bicknell 2003a). The code has already been used in several adiabatic applications (e.g. Saxton et al. 2002a; Saxton, Bicknell & Sutherland 2002b) and most recently in two-dimensional simulations of fully radiative wall shocks (Sutherland, Bicknell & Dopita 2003b). In the latter paper, cooling was dynamically important and the code for preventing numerically unstable shocks was implemented and proved to be important in eliminating physically unrealistic features. We refer to this augmented code as PPMLR.

We have recently ported the PPMLR code to the Message Passing Interface (MPI) environment (see Appendix A). This port enables us to take advantage of the Compaq Alphaserver parallel processor architecture. The MPI port is described in Appendix A. The simulations described here typically involve 16 processors. Future three-dimensional simulations will regularly use 256 processors and, in exceptional circumstances, up to 512 processors.

## 3 SIMULATIONS

In the following subsections we describe a number of simulations that exhibit a wide range of phenomena when we vary fundamental parameters such as the jet energy flux ( $F_E$ ), the jet density ratio ( $\eta$ ) and the filling factor of clouds ( $f_c$ ) obstructing the path of the jet. The jet parameters in the simulations are presented in Table 2, and the characteristics of the clouds and intercloud media are given

<sup>1</sup> See <http://wonka.physics.ncsu.edu/pub/VH-1/>. See also Blondin & Lukin (1993) for the extension of the PPM method to curvilinear coordinates.

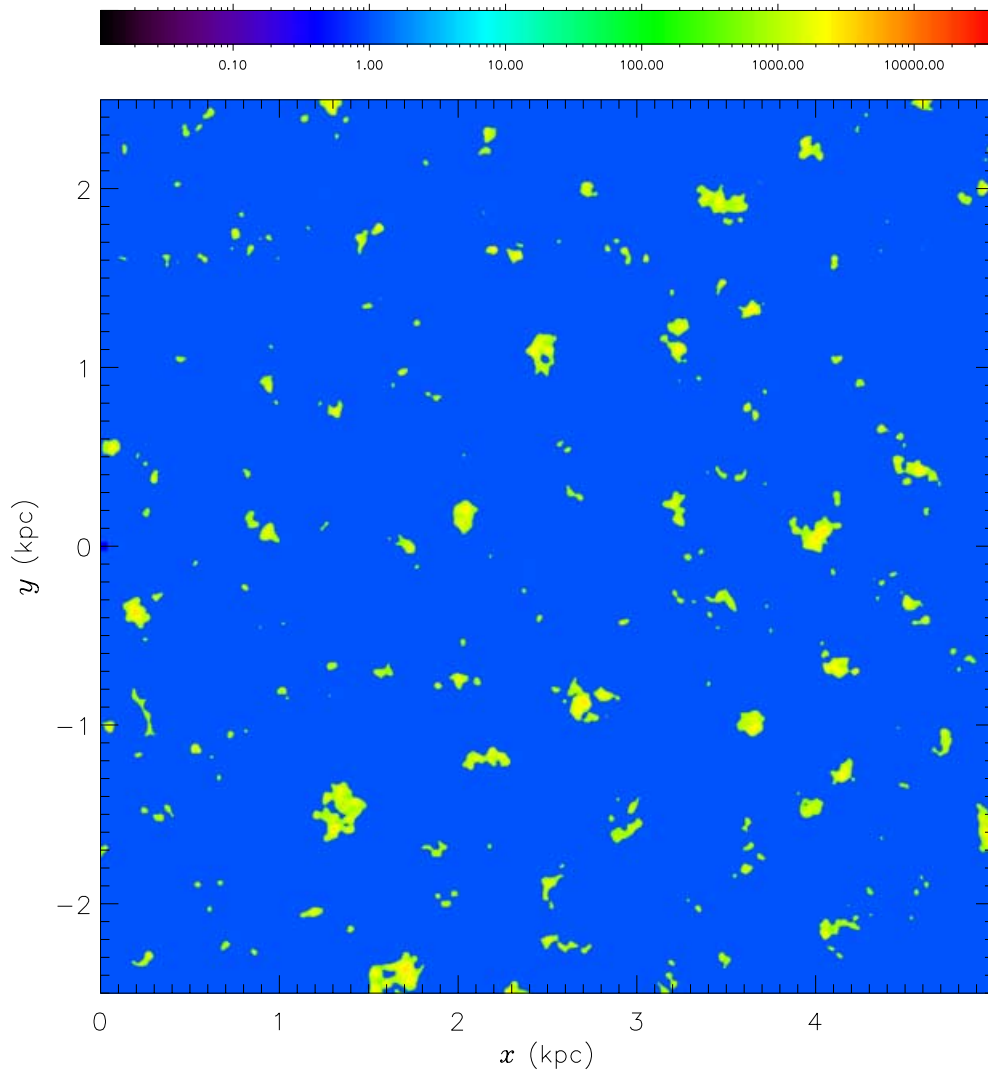


**Figure 1.** Logarithmically scaled map of density relative to the external medium,  $\rho/\rho_x$ , in the initial cloud field of the simulation A1. The dark grey (blue in online version) region represents the intercloud medium and the lighter grey (green) regions represent cloud cells. Each cloud has an internal density structure defined by the Fourier construction described in the text (Section 2.3). The region shown extends over  $5 \times 5 \text{ kpc}^2$  ( $1600 \times 1600$  cells), with the jet origin at the middle of the left edge.

in Table 1. In each simulation the X-ray-emitting intercloud medium has temperature  $T_x = 10^7 \text{ K}$ , and the corresponding isothermal sound speed is our unit of velocity in the simulations,  $v_0 = v_x = 365 \text{ km s}^{-1}$ . Our unit for time measurement is  $t_0 = v_0/1 \text{ pc} = 2.68 \times 10^3 \text{ yr}$ .

The jet is defined by a group of cells on the left boundary where the density, pressure and velocity are kept constant. Elsewhere on the left boundary a reflection condition is applied, representing the effect of bilateral symmetry of a galaxy with equally powerful jet and counterjet. The boundary cells on other sides of the grid are subject to an open boundary condition: in each cycle of the hydrodynamic computation, the boundary cell contents are copied into the adjacent ghost cells. This one-way boundary allows hydrodynamic waves to propagate off the grid.

In a journal paper, one is necessarily limited to showing illustrative snapshots from simulations. Movies of the simulations described in the following section, which show the detailed dynamical evolution, may be obtained from <http://macnab.anu.edu.au/radiojets/>.

### 3.1 Model A1: high-density, overpressured jet

This simulation exhibits both expected and unexpected features of jets interacting with a distribution of clouds in an active nucleus. The jet is initially unimpeded by clouds and generally behaves like a jet in a uniform medium showing the usual bow-shock, terminal jet-shock and backflow. Then two small clouds are overtaken by the bow-shock and the overpressure in the cocoon drives radiative shocks into them. Subsequently the jet backflow is distorted by the reverse shock emanating from the upper of the two clouds. The interaction with the cloud field becomes more dramatic when the apex of the bow-shock strikes one of the larger clouds just below the jet axis. Again this drives a strong radiative shock into the cloud and the larger reverse shock deflects both the jet and backflow sideways. The bow-shock then intersects the larger of the two clouds and this produces an additional reverse shock that deflects the jet further sideways. The jet continues onwards past these two clouds while the dense clouds in the wake of the bow-shock (i.e. immersed within the jet cocoon) are gradually disrupted by the gas surrounding them.

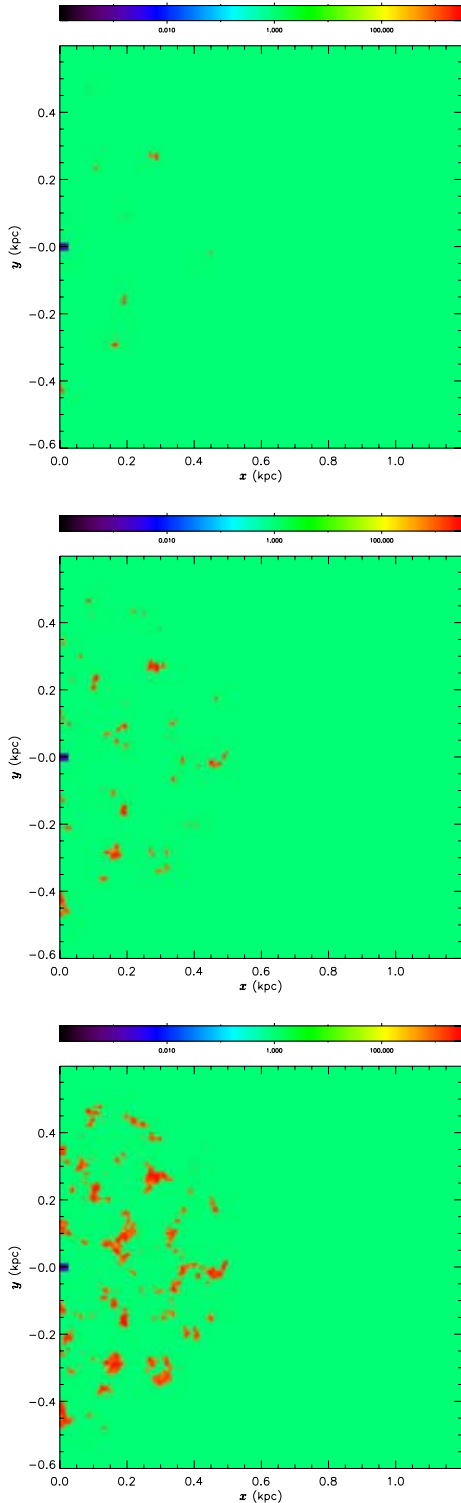


**Figure 2.** Density maps of the initial cloud fields of the simulations B1, B2 and B3 (from top to bottom, respectively). These cloud fields were generated from the same fractal distribution but use a different threshold  $\sigma_{\min}$  to define the cloud/intercloud boundaries. The entire grid covers  $4 \times 4 \text{ kpc}^2$  ( $2000 \times 2000$  cells), but the square subregion shown above is  $1.2 \text{ kpc}$  on a side. The jet origin is at the middle of the left edge of each panel.

A large amount of turbulence is generated within the jet cocoon by the reverse shocks from the bow-shock impacted clouds and the jet flow is clearly affected but not disrupted. At late times many of the clouds immersed within the cocoon show trails resulting from the

ablation of gas within the turbulent cocoon. However, the details of these features will be uncertain until we are able to resolve them fully and subdue the effects of numerical mass diffusion.

Notable features of this interaction are:

- (i) the jet does not directly touch any of the clouds; the radiative shocks within the clouds are all produced as a result of the overpressure behind the bow-shock;
- (ii) the importance of the reverse shocks within the cocoon in deflecting the jet and making the cocoon more turbulent;
- (iii) the survival of the jet despite these interactions (aided by heaviness of the jet in this simulation,  $\eta = 0.3835$ ).

The left-hand panel of Fig. 5 shows the jet interacting with clouds during an early stage of the simulation,  $t = 5t_0$ . The bow-shock and therefore the influence of the jet have only propagated about  $1.7 \text{ kpc}$  forward and  $0.5 \text{ kpc}$  laterally, and most of the clouds remain in their initial condition. The upper panels of Fig. 6 show details of the subregion immediately surrounding the jet at this time of the simulation. Within the high-pressure region bounded by the bow-shock, all clouds are shocked. The cloud shocks are the intensely cooling regions on the cloud perimeters visible in the upper-right-hand panel of Fig. 6. The cloud density is sufficiently high that the shocks have penetrated only a few pc at this stage – a small depth compared to the cloud thickness. The other noteworthy cooling component visible in the cooling map (Fig. 6) is the X-ray emission from the bow-shock. This is more intense near the apex of the bow-shock than at its sides.

The lower panels of Fig. 6 show the density and cooling at a later time,  $t = 10t_0$ , when the jet is more advanced and the clouds are more eroded. Some clouds that lay in the path of the jet at time  $5t_0$  [located at  $(0.85, 0.15) \text{ kpc}$  and  $(0.95, 0.10) \text{ kpc}$ ] are now completely shocked and destroyed. Other clouds have survived closer to the nucleus but with less damage because they are out of the path of the jet, e.g. those at  $(0.3, 0.4) \text{ kpc}$  and  $(0.3, 0.25) \text{ kpc}$ . The jet survives an oblique interaction with one group of eroded clouds near  $(0.9, 0.15) \text{ kpc}$ , but its width increases to the right of this point. A second cloud collision near  $(1.7, 0.0) \text{ kpc}$  deflects the jet into the negative  $y$ -direction, and causes its decollimation into a turbulent bubble of hot plasma accumulating at the apex of the bow-shock. The head of the jet is unsteady and changes direction completely within a few  $t_0$ .

The density distribution at time  $t = 19t_0$ , near the finish of the simulation, appears in the right-hand panel of Fig. 5. Clouds are visible in all stages of shock compression. The two major cloud collisions, around  $(1.00, 0.05) \text{ kpc}$  and  $(1.75, 0.00) \text{ kpc}$ , now leave the jet well collimated and relatively straight. The jet loses collimation at a third collision, around  $(2.5, -0.2) \text{ kpc}$ . The turbulent bubbles around the head of the jet have grown, and spurt between the clouds in several different directions. As was the case at  $t = 5t_0$  and  $10t_0$ , the clouds situated off to the sides have survived much better than clouds that lay close to the direct path of the jet.

In summary, whether a cloud behaves radiatively and contracts, or adiabatically and ablates, is affected by its size, location and density. Small clouds are more effectively adiabatic and less durable than large clouds. This may be partly because their exposed surfaces are large compared to their internal volume, and partly because they are geometrically narrower and on average less dense than large clouds. Some of the smallest swell and develop ablative tails almost as soon as they enter the cocoon, e.g. those between  $(1.3, -0.7) \text{ kpc}$  and  $(2.1, -0.7) \text{ kpc}$  when  $t = 10t_0$ , in Fig. 6. A larger cloud near  $(0.2, -0.5) \text{ kpc}$  was within the cocoon for most of the simulation and yet it was barely affected, even until  $t = 19t_0$  (right-hand panel, Fig. 5).

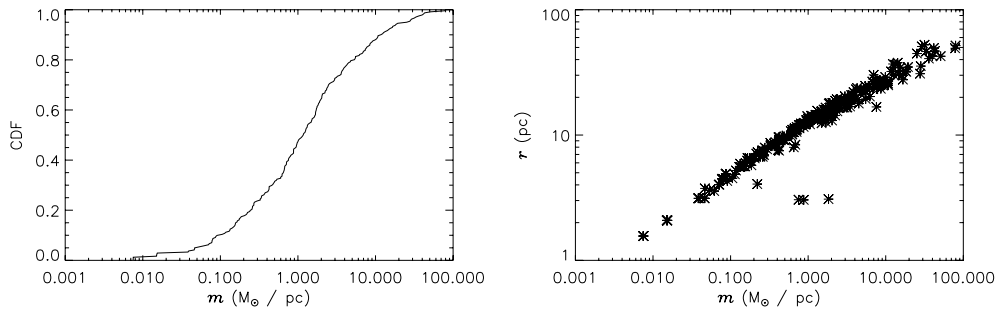


**Figure 3.** Initial characteristics of the cloud populations in model A1 ( $\sigma_{\min} = 1.9$ ). The left column shows a cumulative distribution function of the individual cloud masses per pc. The right column presents a scatter plot of the characteristic depth versus cloud mass per pc.

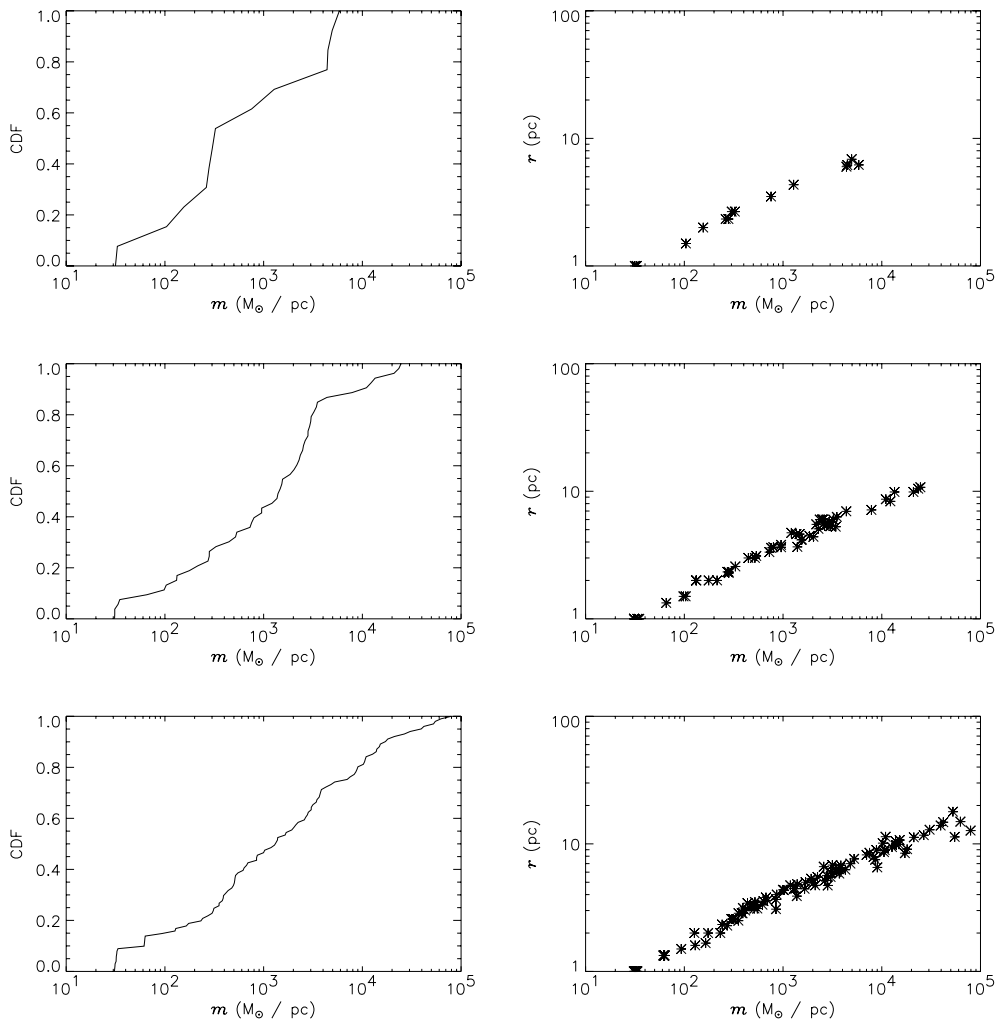


**Figure 4.** Cumulative distribution function of cloud masses (left-hand panel) and mass versus thickness relation (right-hand panel) as in Fig. 3 but for the models B1 ( $\sigma_{\min} = 2.6$ ), B2 ( $\sigma_{\min} = 1.9$ ) and B3 ( $\sigma_{\min} = 1.2$ ), from top to bottom, respectively.

Qualitatively, each cloud appears to suffer one of three possible fates. Small clouds are destroyed quickly regardless of their position. Large clouds near the path of the jet affect the jet through reflection shocks (even if the jet does not strike directly) but they inflate and ablate away in the long term. Large bystander clouds situated well off the jet axis endure almost indefinitely.

Interaction with clouds alters the propagation and shape of the bow-shock. The bow-shock is severely retarded when it strikes a

cloud and refracts through the gaps between clouds. Thus the bow shock surface is conspicuously indented (‘dimpled’) for as long as it remains amidst the cloud field. We would expect this effect to manifest in 3D simulations also, although the extra degree of freedom in 3D is also likely to bring about some differences.

The jet generally remains identifiable and collimated after deflection in two or at most three cloud interactions. These interactions need not be direct: it is sufficient for the jet to interact with the

**Table 2.** Parameters and properties of the jets in the respective simulations.  $M$  = Mach number,  $\eta$  = ratio of jet density to intercloud medium density,  $\xi$  is the ratio of the initial jet pressure to the pressure of the external medium, and  $r_j$  is one-half the extent of the slab-jet (the slab-jet ‘radius’). An equivalent three-dimensional jet with circular cross-section has mass flux  $\dot{M}$ , thrust  $\Pi$  and power  $F_E$ .

Model	$M$	$\eta$	$\xi$	$r_j$ (pc)	$\dot{M}$ ( $M_\odot \text{ yr}^{-1}$ )	$\Pi$ ( $10^{33}$ dyn)	$F_E$ (erg s $^{-1}$ )	$\dot{M}$ $/A_j \rho_x v_x$	$\Pi$ $/A_j \rho_x v_x^2$	$F_E$ $/A_j \rho_x v_x^3$
A1	12.7	0.384	947	25	$3.5 \times 10^{-2}$	5.43	$10^{45}$	313	$2.10 \times 10^4$	$2.10 \times 10^8$
B1	12.7	$1.16 \times 10^{-3}$	100	10	$1.0 \times 10^{-2}$	9.17	$10^{46}$	5.58	$2.22 \times 10^3$	$1.31 \times 10^8$
B2	12.7	$1.16 \times 10^{-3}$	100	10	$1.0 \times 10^{-2}$	9.17	$10^{46}$	5.58	$2.22 \times 10^3$	$1.31 \times 10^8$
B3	12.7	$1.16 \times 10^{-3}$	100	10	$1.0 \times 10^{-2}$	9.17	$10^{46}$	5.58	$2.22 \times 10^3$	$1.31 \times 10^8$
B3a	12.7	$1.16 \times 10^{-3}$	100	10	$1.0 \times 10^{-2}$	9.17	$10^{46}$	5.58	$2.22 \times 10^3$	$1.31 \times 10^8$

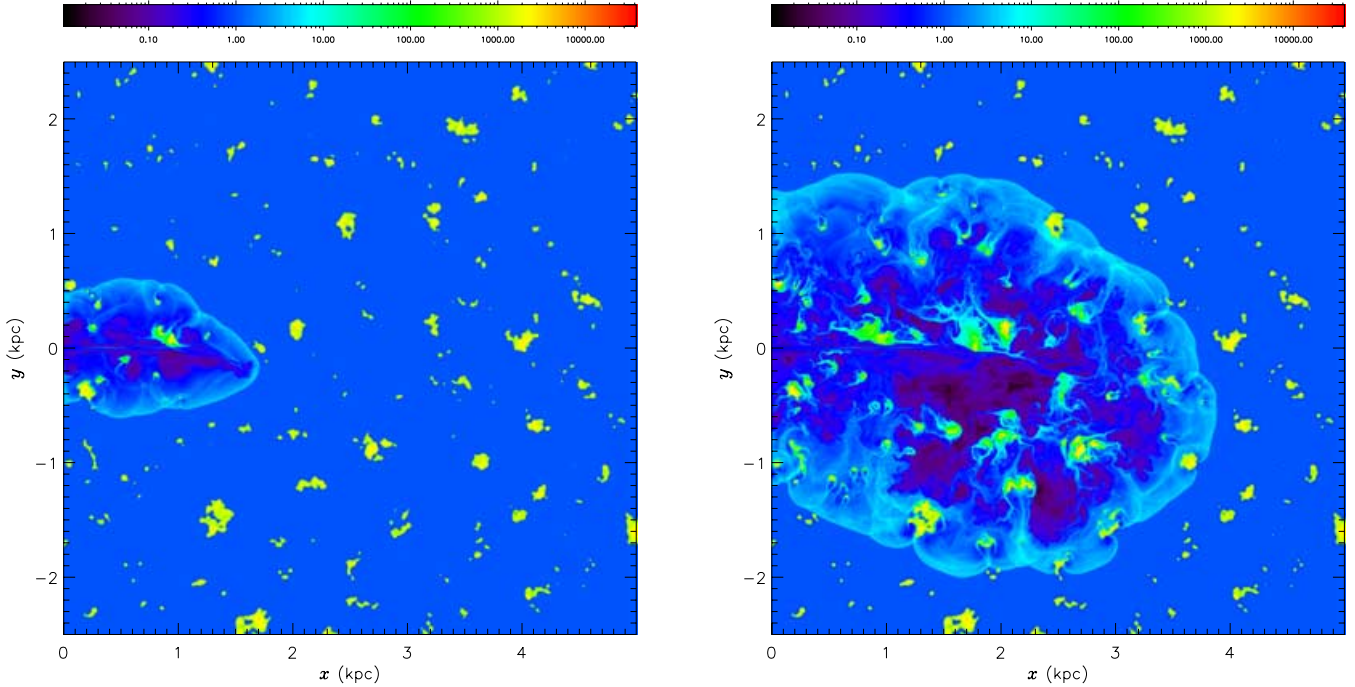


**Figure 5.** Logarithmically scaled map of  $\rho/\rho_x$  in the model A1 at time  $t = 5t_0$  (left-hand panel) and  $19t_0$  (right-hand panel). The intercloud medium has number density  $n_x = 0.01 \text{ cm}^{-3}$ .

reverse shocks that reflect off a cloud lying within several times  $r_j$  off the path of the jet. These backwashing shocks spread continually in the turbulent cocoon; they appear to act like a ‘cushion’ against collision between jet and cloud. More than three consecutive cloud interactions disrupts the jet.

### 3.2 Low density, overpressured jets

#### 3.2.1 Jet stability properties, model B0

Our main series of simulations depicts a more powerful jet ( $F_E = 10^{46} \text{ erg s}^{-1}$ ) with a much lower density contrast ( $\eta = 1.16 \times 10^{-3}$ ) and a large overpressure ( $\xi = 100$ ). The initial internal Mach number of the jet is  $M = 12.72$  at the nucleus. The jet radius is  $r_j = 10 \text{ pc}$ , the square grid is  $4 \text{ kpc}$  wide and the resolution is  $2000 \times 2000$  cells. The background gas again has a temperature  $T_x = 10^7 \text{ K}$  but the density is raised to  $n_x = 1 \text{ cm}^{-3}$ . These parameters are suggested by the observations of GPS sources (e.g. in the summary by Conway 2002b).

One of the aims of this work is to distinguish the effects of an inhomogeneous medium from the phenomena that are intrinsic to

the jet itself. Therefore we have performed a control simulation containing only the jet and an initially uniform intercloud medium. The main large-scale features at the end of this simulation (see Fig. 7) are: an outer shell of highly overpressured gas processed through the bow-shock, enclosing a turbulent cocoon where jet plasma mixes with external gas. The length of the jet is small compared to the diameter of the bubble surrounding it. The jet is highly unstable: it stays recognizably straight throughout its first  $0.1 \text{ kpc}$  but at greater distances from the origin it flaps transversely with increasing amplitude, losing collimation at positions beyond  $\sim 0.5 \text{ kpc}$  from the origin. This highlights a feature of two-dimensional simulations that may not be present in three dimensions. The instability in this jet is driven by 2D turbulence in the cocoon that results from the mixing of gas at the edge, although the instability is not as rapid as in the ensuing cases with cloudy media. The turbulent driving is probably stronger here because of the persistence of vortices associated with the well-known inverse cascade in two dimensions. The instability evident here is seeded by a very small amount of numerical noise in the initial data.

Hardee & Norman (1988) performed a linear stability analysis of the instabilities of two-dimensional slab-jets. Two qualitative

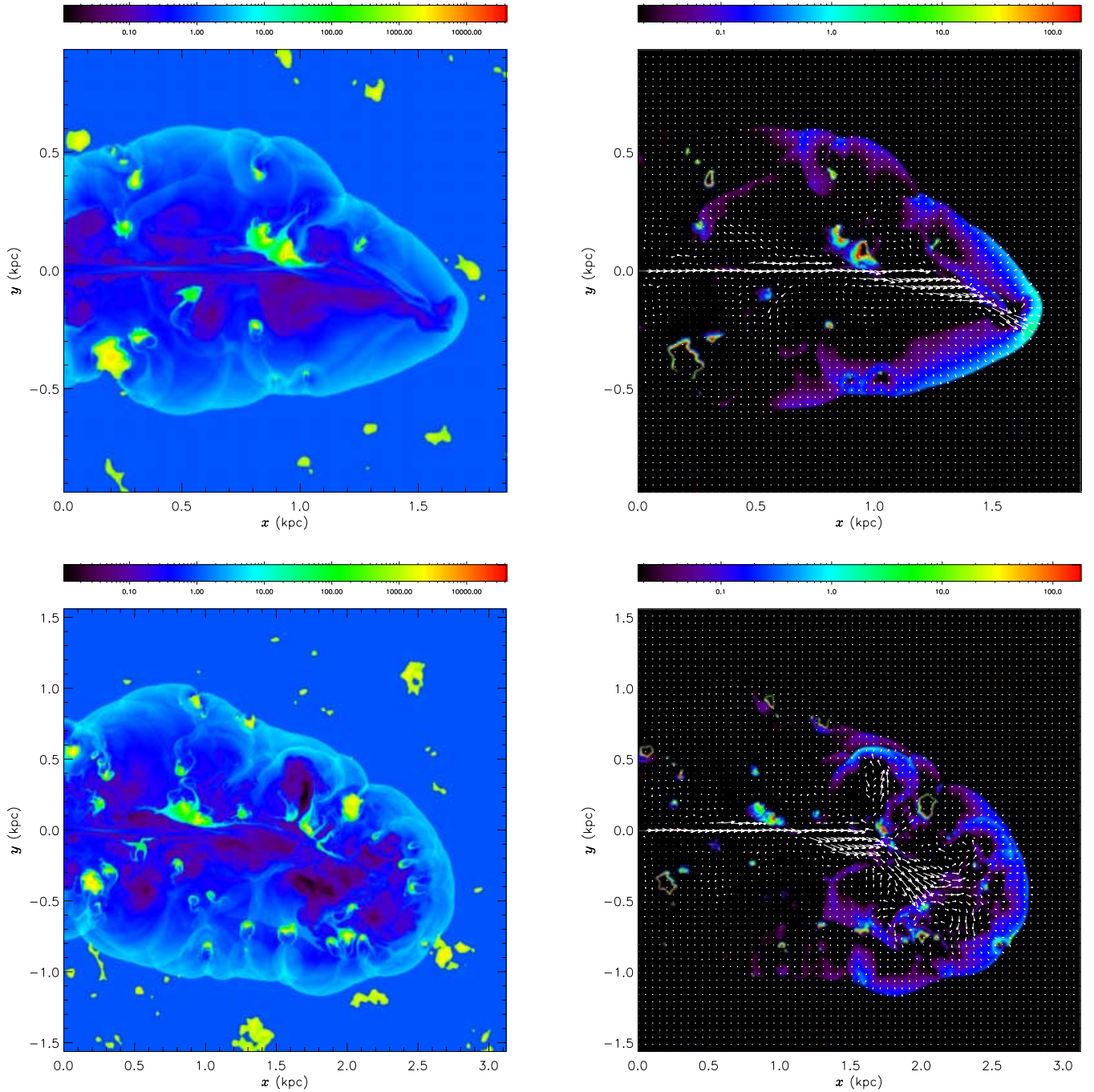


**Figure 6.** Subregions of model A1 showing the area disturbed by the jet at times  $t = 5t_0$  (upper row) and  $10t_0$  (lower row). The left-hand panels show density  $\rho/\rho_x$  and the right-hand panels show velocity vectors superimposed on maps of the volumetric rate of cooling. The cooling is measured in units of  $\text{erg cm}^{-3} \text{s}^{-1}$ , but the upper end of the scale is deliberately saturated to keep the bow-shock visible. The actual maximum rate of radiative cooling in the cloud shocks is  $1.8 \times 10^3 \text{ erg cm}^{-3} \text{ s}^{-1}$  when  $t = 5t_0$ . Reflected and refracted shocks are visible at distances of order 10 pc around some of the clouds.

kinds of instabilities occur. An unstable pinching mode is responsible for diamond shocks at quasi-periodic locations along the length of the jet. Sinusoidal instabilities are responsible for transverse oscillations, which disrupt and ultimately decollimate the jet. According to the analytical and numerical results of Hardee & Norman (1988), the maximally growing fundamental mode has wavelength

$$\lambda^* \approx \frac{0.70}{\alpha_{\text{sj}}} \frac{2\pi M r_j}{0.66 + \eta^{1/2}}, \quad (10)$$

an  $e$ -folding length-scale of

$$l_e^* \approx \frac{1.65}{\alpha_{\text{sj}}} M r_j, \quad (11)$$

and angular frequency

$$\omega^* \approx 1.5 \alpha_{\text{sj}} a_e / r_j, \quad (12)$$

where  $a_e$  is the adiabatic sound speed in the cocoon immediately exterior to the jet surface, the parameter  $\alpha_{\text{sj}} \rightarrow 1$  for  $M \gg 1$ , and  $\eta$ ,

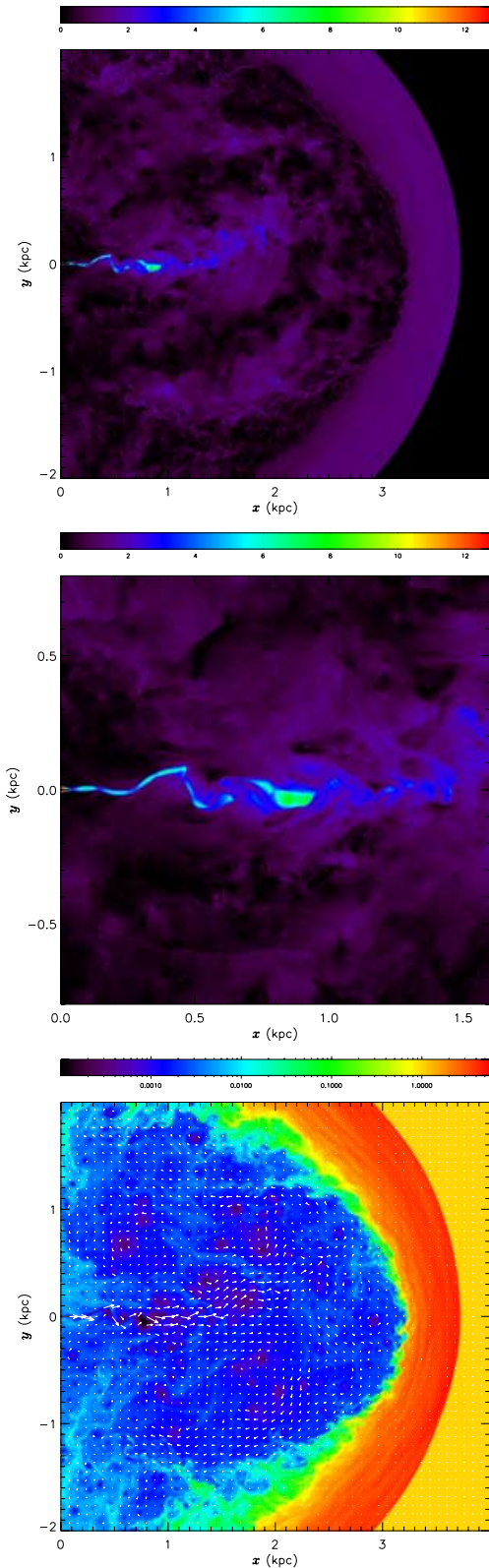


**Figure 7.** Snapshots of the cloudless test model B0 at time  $t = 48t_0$ . The upper panels show the local Mach number: the full computational grid, and a subregion around the jet. The lower panel maps density,  $\rho/\rho_x$ , overlain with velocity vectors.

in this case, is the density contrast between the jet and its immediate surroundings within the cocoon.

In simulation B0, the internal Mach number within the jet is reduced to typically  $M \approx 6$ , downstream of the first diamond shock (see Fig. 7). The cocoon gas immediately surrounding the jet has a density typically  $\sim 4\rho_j$  and adiabatic sound speed  $a_e \sim 800v_0$ , where  $v_0 \approx 365 \text{ km s}^{-1}$  is the isothermal sound speed of the undisturbed medium outside the bow-shock. Upon substitution into equations (10) and (11), these values imply exponential growth of sinusoidal instabilities on scales  $l \sim 100 \text{ pc}$  and with wavelengths  $\lambda \sim 200 \text{ pc}$ . This is consistent with the growing oscillations that are apparent in individual frames of our simulations, e.g. in Fig. 7. From equation (12), the implied period of the instability is  $T^* < 0.052t_0$ . The simulated jet thrashes back and forth transversely within this typical time.

The sinusoidal transverse instability revealed in this homogeneous ISM simulation are similar in wavelength and growth time to instabilities manifest in the inhomogeneous simulations discussed below. However, the appearance of this instability in this ‘clean’ simulation shows that the instability can be properly regarded as a Kelvin–Helmholtz (KH) instability of the jet itself – albeit, in the inhomogeneous cases, stimulated by the turbulence in the cloudy medium. Note that growth and wavelength of the transverse KH instability at first sight seems to be suggestive of a transonic jet. However, the comparison with the Hardee & Norman (1988) expressions for maximally growing wavelength and growth time shows that our simulations are consistent with the expected behaviour of *supersonic* jets with the quoted Mach numbers.

### 3.2.2 Small cloud filling factor: model B1

This is our simulation with the fewest clouds: their filling factor is  $f_c = 4.1 \times 10^{-3}$  ( $\sigma_{\min} = 2.6$ ) within a region spanning radially between 0.1 and 0.5 kpc from the nucleus. All of the clouds are quickly overtaken by the expanding bow-shock. As in model A1, each cloud is shocked by the overpressure of the cocoon (up to  $5 \times 10^4$  times greater than the external pressure), and contracts as it cools radiatively. Some clouds are accelerated away from their initial positions by the thrust of the jet. For some other clouds, radiative cooling eventually proves inadequate; the tendency to contract is overcome, and the fate of the cloud is expansion and ablation. Half-way through this simulation at time  $t = 24t_0$ , Fig. 8, top panel, shows the destruction of one such cloud in the path of the jet, situated at (0.6, 0.0) kpc but ablating away across about 0.2 kpc to the right. Meanwhile, a few extremely dense and compact clouds persist in apparent safety off to the sides of the jet, within a few hundred pc of the nucleus. They appear to survive indefinitely and appear scarcely changed by the time the simulation ends, as seen in the middle panel of Fig. 8. In comparison with Fig. 7 we see much more dense gas (derived from the ablated clouds) intermixed with jet plasma in the cocoon.

The last panel in Fig. 8 represents the appearance of the jet in synchrotron emission at late stages of the simulation. Here we have used the approximation (e.g. Saxton, Sutherland & Bicknell 2001; Saxton et al. 2002a) that the emissivity  $j_v \propto \varphi p^{(3+\alpha)/2}$ , where  $p$  is the pressure,  $\varphi$  is the relative concentration of mass originating from the jet (a scalar tracer that is passively advected in our code) and  $\alpha$  is the spectral index that we take to be 0.6. Several diamond shocks are visible in the well-collimated section of the jet closest to the nucleus. The brighter, barred ‘fishbone’ shaped pattern seen at distances  $x > 0.4 \text{ kpc}$  is a transient and typical manifestation of the transverse instability of the jet (as in Section 3.2.1).

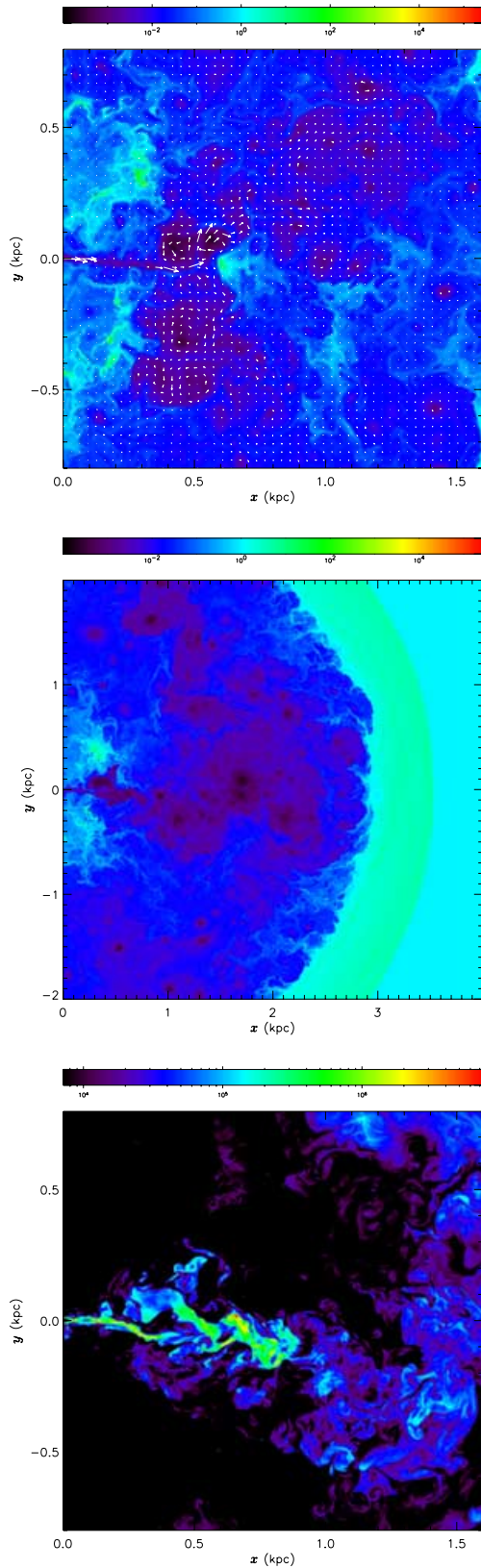


**Figure 8.** Snapshots of model B1. Top:  $\rho/\rho_x$  and velocity field in a sub-region at time  $t = 24t_0$ . Middle:  $t = 48t_0$ ,  $\rho/\rho_x$  in the full grid. Bottom:  $t = 48t_0$ , simulated radio emissivity in a subregion (the lowest background intensity is  $1/1024$  times the peak).

### 3.2.3 Intermediate cloud filling factor: model B2

In this case the filling factor of clouds is higher with  $f_c = 3.0 \times 10^{-2}$ , corresponding to  $\sigma_{\min} = 1.9$ . In the first few  $t_0$  of simulation time the jet is completely disrupted within  $< 0.1$  kpc of the nucleus as a result of the KH instability induced by waves reflected off the innermost clouds. By  $t \sim 12t_0$  (see top panel, Fig. 9), the jet has ablated the nearest clouds and cleared an unobstructed region out to  $\sim 0.1$  kpc on either side. Within this region the jet remains well collimated during the rest of the simulation. The clouds that define the sides of this sleeve are shocked but they survive until the last frame (middle panel, Fig. 9). The flow of plasma from the head of the jet splits into a fork on either side of a cloud group that sits nearly on the jet axis at about  $x \approx 0.5$  kpc. Throughout the simulation these clouds retain dense, efficiently cooling cores but they continually lose dense gas entraining into the stream of jet plasma passing to either side. Near the end of the simulation ( $t = 48t_0$ , Fig. 9) these obstructive clouds are trailed by dense ablated gas extending throughout a triangular area up to 0.5 kpc further out in the positive  $x$ -direction.

The radio emissivity (last panel, Fig. 9) has some similarities to the appearance of model B1, with a bright jet remaining well collimated out to around 0.5 kpc. However the turbulent plumes of jet-derived plasma beyond the head of the jet are more disrupted by the dense obstructions of the cloud field; radio bright plasma divides in several directions, as Fig. 9 shows. The brightest areas of the jet and post-jet flows are typically concentrated closer to the nucleus than in the less cloudy model B1.

### 3.2.4 Large filling factor: model B3

This is our simulation with largest filling factor of clouds,  $f_c = 0.12$  and  $\sigma_{\min} = 1.2$ . As a result of the high coverage of clouds, the jet is disrupted when it is less than 0.1 kpc from its origin. Jet plasma streams through the available gaps between the persistent clouds (see the density distribution in right-hand panel of Fig. 11 below). These low-density, radio-bright channels evolve as the cloud distribution changes. A channel may close when nearby clouds expand ablatively or are blown into positions where they create a new obstruction. Turbulent eddies of jet plasma accumulate in pockets within the cloud field, most conspicuously in places where a channel has closed. The density image, Fig. 10, illustrates the initial development of intercloud channels.

The left-hand panel of Fig. 11 shows simulated radio emissivity in the inner regions of the galaxy at the end of the simulation. The radio-bright material is concentrated near the nucleus within an irregular, branched region that is not directly related to the alignment of the initial jet. This particular configuration of channels is ephemeral, occurring after the opening and closure of previous channels as the cloud field evolves.

Eventually, one or more channels pushes into the open region outside the cloudy zone. A spurt of turbulent jet plasma accumulates at that point. In later stages of our simulations, these eruptions eventually become large compared to the cloudy zone, and merge with adjacent eruptions to form a diffuse, turbulent, approximately isotropic outer cocoon composed of a mixture of jet plasma, ablated cloud gas and intercloud gas processed through the bow-shock.

### 3.2.5 Effect of cooling: model B3a

We ran a further simulation with the same cloud field as in B3 but with radiative cooling switched off (see Fig. 12). In the absence of radiative cooling, the compression of clouds is insignificant. The

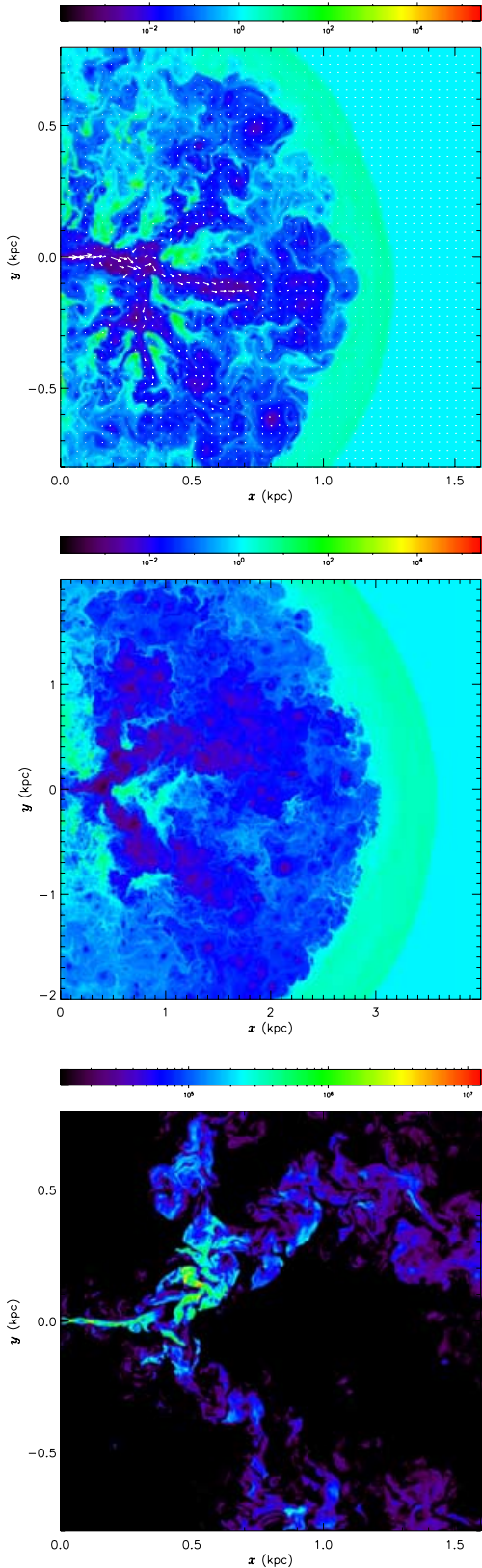


**Figure 9.** Snapshots of model B2. Top:  $\rho/\rho_x$  and flow velocities near the jet when  $t = 12t_0$ . Middle:  $t = 48t_0$ ,  $\rho/\rho_x$  throughout the full grid. Bottom:  $t = 48t_0$ , simulated radio emissivity around the jet (with a dynamic range of 1024).

outflow of jet plasma rapidly turns the clouds into ablating, flocculent banana shapes. Large clouds and small clouds ablate efficiently. The survival time of individual clouds is shorter than in the simulation including the effects of radiative cooling. Dense material is more readily ablated from the clouds, and this may block channels of jet plasma more readily or at an earlier time, but otherwise the radio morphology is qualitatively similar to that of B3.

### 3.3 Evolution of the outer part of the radio source

In each case, as a consequence of the disruption of the jet, its momentum is distributed throughout the cocoon in an isotropic way. Hence, the long-term evolution is similar to that of an energy-driven bubble. Fig. 13 presents plots of the average radius of the furthestmost extent of the radio plasma versus time, for representative simulations. The plots also show the corresponding analytic solution for a two-dimensional bubble with the same parameters of energy flux per unit length and density (grey line, see Appendix B for a derivation). It is evident that the analytic slope of the radius–time curves is replicated very well by the simulations. The offset may be attributed to the time taken for the isotropic phase to be established. This may be related to the finite minimum width of the jet at its nozzle, the size of the innermost nuclear region that is initially cloudless, and the intrinsic length-scale of the instability of the jet (Section 3.2.1).

We expect that a similar power-law expansion will occur in three dimensions, although this of course is yet to be confirmed. However, given that jet momentum and power can be redistributed isotropically in three dimensions, it is reasonable to expect that the long-term evolution of the outer bubble will be described by a three-dimensional energy-driven bubble.

## 4 COMPARISON OF MODEL B1 WITH 3C 48

While these simulations have been two-dimensional, some of their features should persist in three-dimensional simulations with similar parameters. In particular the trends with filling factor will probably persist, to some extent, so that comparisons with existing observations are of interest, even at this stage. We therefore make a tentative comparison of one of these simulations (model B1) with the CSS quasar 3C 48. We can also draw some general conclusions from these simulations, concerning the likely overall morphology of young radio sources.

Simulation B1 has the lowest filling factor of dense clouds and impedes the jet the least. The jet is still disrupted but the flow associated with it continues with reduced collimation and with its forward momentum spread over a much larger region. In the disrupted section, transverse oscillations are produced, with shocks created at points where the jet bends significantly, leading to local enhancements in emissivity. A large-scale bubble is produced outside the cloudy region but the jet also retains some coherency in the intermediate region. This particular simulation bears a strong qualitative resemblance to 3C 48. In Fig. 14 a snapshot of the simulated radio emissivity at a particular time is compared with the 1.6-GHz VLBI image of 3C 48 (Wilkinson et al. 1991). In two dimensions, the alternating direction of the jet results from the transverse instability that we have already discussed (Section 3.2.1). In three dimensions, the corresponding instability would be a helical  $m = 1$  mode. In both cases the alternating direction of the supersonic flow produces shocks. We see evidence for these, in both the snapshot of the emissivity from the 2D simulation and the image of the jet.

This particular simulation predicts that there will be a diffuse halo of emission external to the jet region of the source. This was,

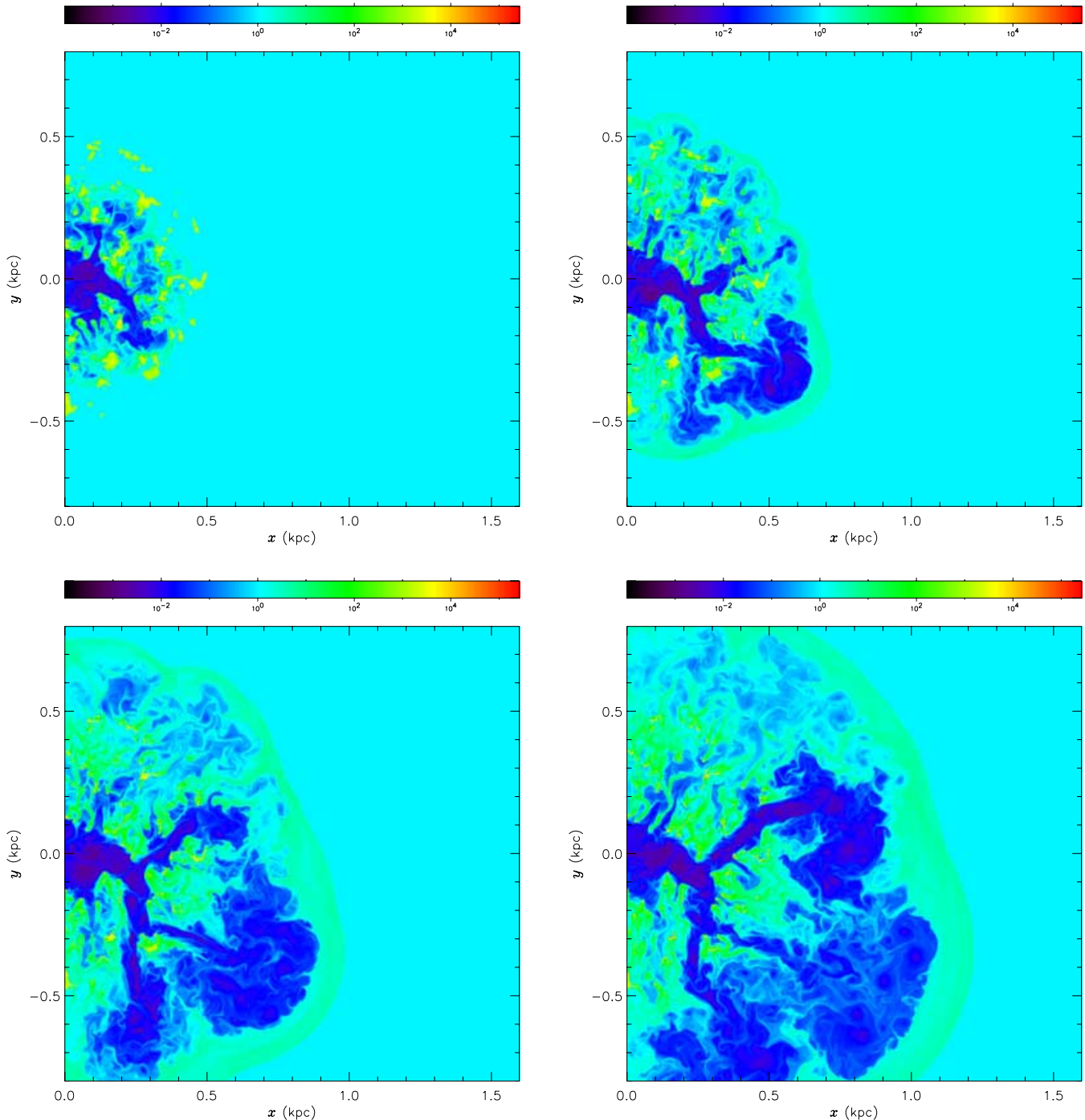


**Figure 10.** Logarithmically scaled density images ( $\rho/\rho_x$ ) of a central subregion of simulation B3 during the initial erosion of channels of jet plasma, and the earliest eruptions of radio bubbles beyond the surface of the cloudy zone. The time steps are  $t = 3t_0, 6t_0, 9t_0, 12t_0$  in the top-left, top-right, bottom-left and bottom-right frames, respectively.

in fact, detected in larger scale images of 3C 48. One such image, presented in Wilkinson et al. (1991), shows diffuse emission on a 1-arcsec scale in 3C 48 extending well beyond the compact jet structure evident in the VLBI image. More recent higher quality images have been obtained by Ojha et al. (in preparation) and one of their contour maps is reproduced in Fig. 14. These images clearly reveal the extended structure of 3C 48. Wilkinson et al. (1991) had already concluded that the morphology of 3C 48 is likely the result of

jet–cloud interactions and cited evidence for asymmetric emission-line gas north-west of the core as well as the presence of dust revealed by the high *IRAS* flux. They interpreted the radio knot close to the core as the result of a jet–cloud interaction. While this is possible, our simulation shows that the sort of jet disruption observed in 3C 48 can occur without direct jet–cloud encounters. The general turbulence in the jet cocoon can excite jet instabilities, producing shocks in the supersonic flow either as a result of the jet being bent through

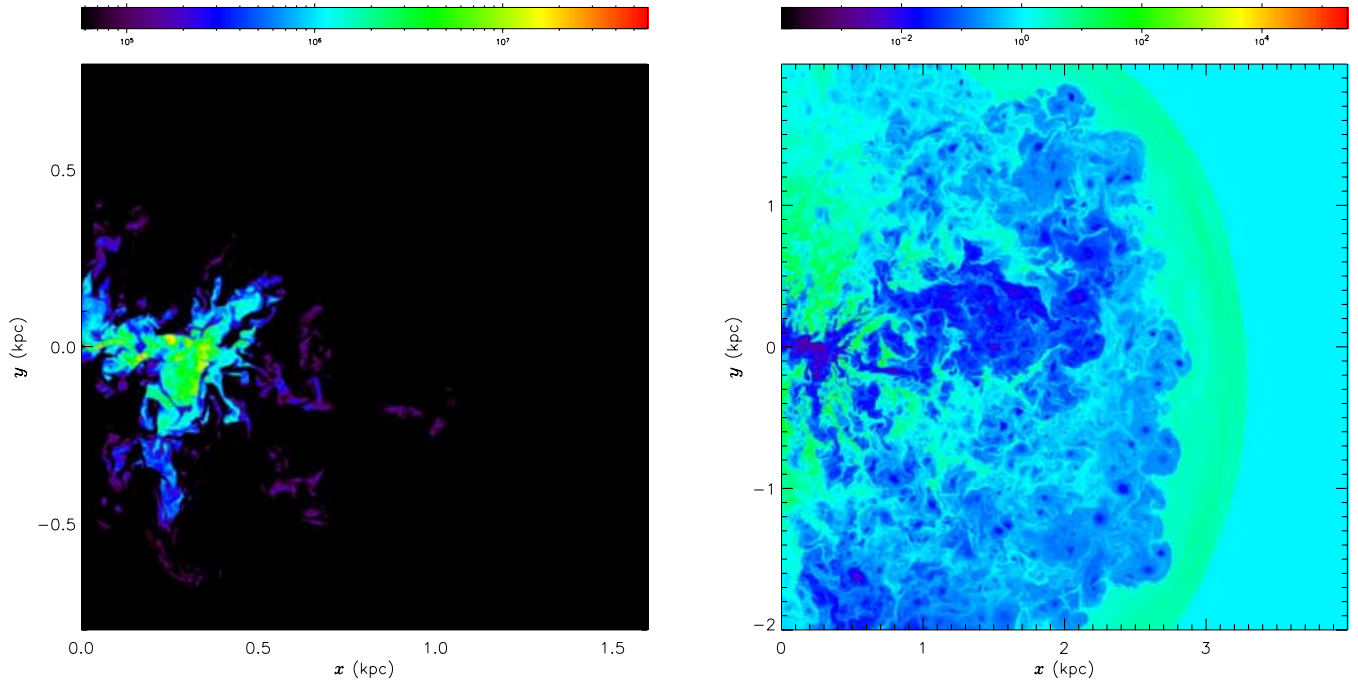


**Figure 11.** The final condition of model B3 ( $t = 48t_0$ ), comparable to the lower panels of Figs 8 and 9. The left-hand panel is a simulated radio emissivity image of the vicinity of the jet, with dynamic range 1024 as in previous figures. The right-hand panel represents  $\rho/\rho_x$  throughout the full grid.

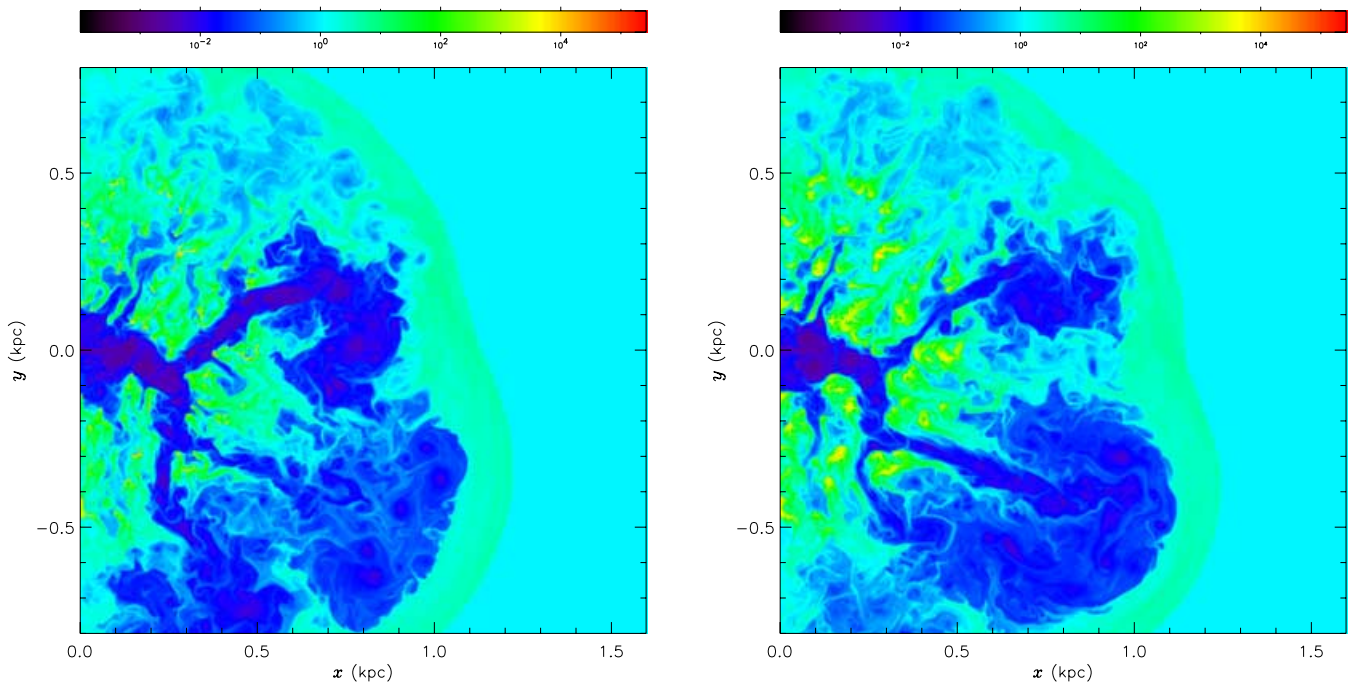


**Figure 12.** Demonstration of the effects of radiative cooling upon cloud survival. Density frames ( $\rho/\rho_x$ ) are compared at time  $t = 12t_0$ , with the left-hand panel showing simulation B3 and the right-hand panel shows simulation B3a, which is the equivalent simulation with radiative cooling switched off. In the absence of radiative cooling, clouds expand and ablate rapidly as soon as they pass through the bow-shock.

an angle greater than the Mach angle, or through pinching-mode instabilities. (Both of these occur in the simulations.) An explanation for the first bright knot involving cocoon turbulence may therefore be more favourable since direct jet–cloud encounters are usually highly disruptive and Wilkinson et al. (1991) appealed to a glancing

deflection in order to explain the radio structure. Given that the sort of jet–ISM interaction revealed in our simulations is occurring, we expect that the emission-line gas would show evidence for shock excitation as a result of radiative shocks induced by the overpressured radio cocoon. Chatzichristou (2001) has suggested that the

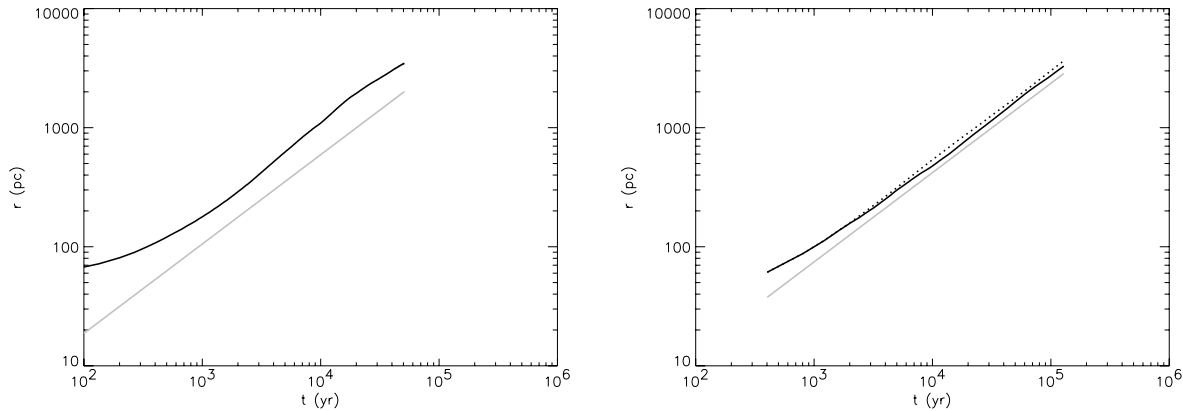


**Figure 13.** Evolution of the mean radius of the bow-shock compared with the radial growth of an equivalent energy-driven bubble model. The left-hand panel shows results for the simulation A1; the right-hand panel shows results for model B3. In each case the grey line is the ideal model, and the black line shows simulation results. The dotted line in the right-hand panel shows the cloudless control model B0.

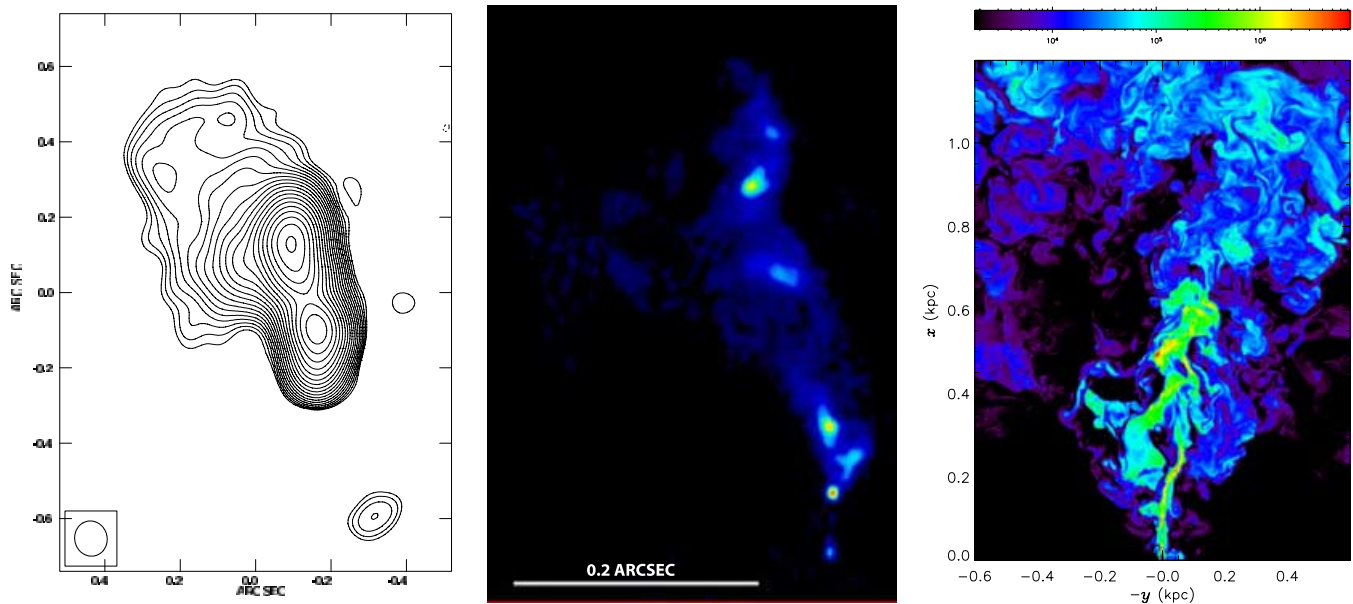


**Figure 14.** The radio features of 3C 48 compared with simulation B1. The left-hand panel is a 22-GHz (*K*-band) VLA A-array image illustrating the large-scale (arcsecond scale) structure of 3C 48 (Ojha, in preparation). This image shows diffuse emission on a larger scale to that of the jet, consistent with the prediction of the simulation. The middle panel is a 1.6-GHz VLBI image featuring the jet and bright knots (Wilkinson et al. 1991). At the redshift of 3C 48 ( $z = 0.3670$ ) an angular scale of 0.1 arcsec corresponds to 0.514 kpc (assuming  $H_0 = 70 \text{ km s}^{-1} \text{ Mpc}^{-1}$ ,  $\Omega_m = 0.27$  and  $\Omega_\Lambda = 0.73$ ). The right-hand panel shows a snapshot of radio emissivity from the B1 simulation, at time  $t = 48t_0$ . Left-hand and middle images are reproduced with the kind permission of R. Ojha and P. Wilkinson, respectively. Middle image reprinted with kind permission from Nature (first appeared in Nature, Vol. 352, p. 313; see <http://www.nature.com>).

emission-line spectrum of 3C 48 may show evidence for a mixture of AGN and shock excitation.

Wilkinson et al. (1991) also noted out that 3C 48, classified as a CSS quasar, is much less extended than other similar power radio-loud quasars. They speculated that the confinement results from the emission-line gas and dust inferred to be present in the ISM. Qualitatively, we agree with this, except to point out that the dispersion of the momentum flux (by a small number of clouds) prevents a radio source from expanding rapidly. As we have shown, the source becomes an expanding bubble with a much slower rate of expansion than a jet with the same kinetic power. Hence the gas and dust is not required to physically confine the radio plasma. The slower expansion can be effected by a small filling factor of dense clouds that redistribute the jet momentum isotropically.

We also note a qualitative resemblance between the simulation B3 and M87. The channelling of the flow in B3 produces a hierarchy of structures resembling the hierarchy of radio structures in M87 apparent in the low-frequency radio image (Owen, Eilek & Kassim 2000). However, we have not emphasized this with a detailed comparison since the scale of the source and the simulation are quite different. Nevertheless, the production of the structure observed in simulation B3 depends mainly on the filling factor of the clouds and this mechanism should also work on larger scales. We propose to confirm this in future with a fully relativistic 3D simulation.

Other sources with similar morphology to 3C 48 and which may be being disrupted in a similar way include the TeV  $\gamma$ -ray blazars, MKN 501 and MKN 421. The most recent VLBI images of these sources (Piner et al. 1999; Giovannini et al. 2000) show similar

structures in the form of disrupted jets and large-scale plumes, suggesting that these sources are disrupted on the subparsec scale by a cloudy medium. Again the scale of the simulation B1 is such that it does not strictly apply. However, the physical principle of these jets being disrupted by a small filling factor of dense clouds is probably still valid with interesting repercussions for the production of the  $\gamma$ -ray emission (Bicknell et al. 2005).

## 5 DISCUSSION

We have presented a series of two-dimensional simulations of slab-jets propagating through inhomogeneous media. Despite the limitations of the restrictions to two dimensions, and to non-relativistic flow, these simulations provide useful insight into the characteristics of jets in radio galaxies which have an inhomogeneous interstellar medium. These include GPS and CSS radio sources, high-redshift radio galaxies and galaxies at the centre of cooling flows. In all of these galaxies there is ample evidence for dense gas clouds that may interact with the radio source producing at least some of the features evident in our simulations. In the case of GPS and CSS sources the inhomogeneous medium may be the result of a fairly recent merger; in the case of high-redshift radio galaxies an inhomogeneous medium is likely to be the result of the galaxy formation process at those epochs, as large galaxies are assembled from sub-galactic fragments.

As well as the limitations to two dimensions and non-relativistic flow, there is another feature of our simulations that requires some comment and that is the ablation of cloud material that is evident in most cases. There is likely to be a large contribution of numerical mass diffusion due to the very high-density contrasts between jet and cloud gas. Although this has some effect on the evolution, the dominant processes in the case of a low filling factor are waves emanating from the clouds impacted by the high-pressure cocoon and, in the high filling factor simulations, direct obstruction of the flow plus wave effects.

Despite the above-mentioned caveats, we have been able to deduce the following general features from our simulations.

(i) **Jet instability.** When propagating through the type of inhomogeneous interstellar medium that we have imposed, the jets become unstable. However, this instability does not always result from direct jet–cloud collisions but occurs indirectly from the waves generated by the impact of the high-pressure jet cocoon on the dense clouds. This leads to a general level of turbulence in the medium that induces unstable Kelvin–Helmholtz oscillations in the jet. An unstable jet was also produced in the homogeneous simulation (B0) and this was related to turbulence caused by the entrainment of ISM into the cocoon as well as the higher level of large-scale turbulence in two dimensions. However, the simulations with an inhomogeneous medium became unstable in a shorter distance and we attribute this to the effect of the clouds.

(ii) **Production of halo/bubble.** The instability of the jet is associated with the spreading of the momentum of the jet and a turbulent diffusion of the jet material into a halo or bubble. These are characteristics that we expect to be present in three dimensions. The radius–time curve for the outer part of the halo is well-described by the analytic expression for a two-dimensional bubble. In three dimensions an energy-driven bubble model should also be appropriate. This is useful since it gives us a way of estimating the energy flux fed into a large-scale radio source from the dimensions of the outer halo and the density of the surrounding interstellar medium. The production of a bubble means that the overall increase of size of the

radio source with time is diminished with respect to a source that propagates unimpeded. However, this restriction on the size of the source is not due to direct physical confinement of the radio plasma by denser gas. Rather, it is the result of the isotropic spread of the jet momentum by the process of jet instability described above.

(iii) **The effect of filling factor.** The main parameter that we have varied in these simulations is the filling factor of the dense clouds and we can see that this makes a considerable difference to the morphology of the radio source. With only a small filling factor of clouds, the jet is readily disrupted, but retains some directed momentum and produces the 3C 48 type morphology described in Section 4. As the filling factor increases, the jet propagates via a number of different channels which open and close leading to a hierarchical structure of radio plasma that we noted is similar to the large-scale structure of M87.

(iv) **The effect of jet density ratio.** We also varied the jet density ratio parameter,  $\eta$ , but only in one simulation. The simulation A1 had  $\eta = 0.38$  whereas in the other simulations  $\eta \sim 10^{-3}$ . The main noticeable effect is that the heavier jet is affected less by instabilities and direct jet–cloud collisions than the lighter jets. This points to an important difference between models with  $\eta \gtrsim 0.01$  and models with  $\eta \lesssim 0.001$ . Of course, such low density ratios are important to provide the relevant power for radio galaxy jets. However, re-assessing for physics but difficult for modellers, such low values of  $\eta$  push models into the relativistic regime, as we have discussed in Section 2.2. There are two important points to be made here. The first is that many jet simulations usually involve a modest value of  $\eta \gtrsim 0.01$  and these may be misleading. Second, the most realistic simulations will be those that directly include relativistic physics and which also incorporate the mixing of relativistic and thermal plasma.

This paper complements other work on the physics of direct jet–cloud collisions (e.g. Wiita, Wang & Hooda 2002; Fragile et al. 2004) in which the focus has been on the effect of a jet on a single cloud. Direct jet–cloud collisions are clearly important in the context of sources such as Minkowski’s object (Van Breugel et al. 1985). In this paper we have clearly been more concerned with the overall radio source morphology, the evolution of an ensemble of clouds, the effects of indirect jet–cloud collisions (i.e. the effect of the high-pressured cocoon on dense clouds) and trends with cloud filling factor. However, we note an interesting connection between Wiita et al. (2002) and this work: we have both noted that less jet disruption occurs in the case of slow dense jets. We also note that the morphology of radiative cloud shocks deduced by Fragile et al. (2004) is also reproduced in some of the individual clouds in our simulations.

Our simulations have clearly all been two-dimensional. What are the expected differences between two-dimensional and three-dimensional work? There are at least two.

(i) In two dimensions, vortices survive for a lot longer as a result of the inverse cascade of turbulent energy. These vortices play a significant role in disrupting the jet and clouds. We expect much less disruption from vortical motions in three dimensions.

(ii) The number of independent directions that the jet can take in three dimensions is greater so that we expect that the clouds will impede the jet less severely and that escape from the cloudy region surrounding the nucleus will be easier.

These issues as well as the inclusion of special relativistic effects will be addressed in future papers.

## ACKNOWLEDGMENTS

Our research has been supported by ARC Large Grant A699050341 and allocations of time by the ANU Supercomputer Facility. Professor Michael Dopita provided financial support from his ARC Federation Fellowship. We are very grateful to P.N. Wilkinson and R. Ojha for their permission to use their respective images of 3C 48. We thank the anonymous referee for the several suggestions improving the format of the paper.

## REFERENCES

- Begelman M. C., 1996, in Carilli C. L., Harris D. A., eds, Proc. Greenbank Workshop, Cygnus A: Study of a Radio Galaxy. Cambridge Univ. Press, Cambridge, p. 209
- Bicknell G. V., 1994, ApJ, 422, 542
- Bicknell G. V., Dopita M. A., O’Dea C. P., 1997, ApJ, 485, 112
- Bicknell G. V., Dopita M. A., Tsvetanov Z. I., Sutherland R. S., 1998, ApJ, 495, 680
- Bicknell G. V., Sefouris V., Saripalli L., Saxton C. J., Subrahmanyan R., Sutherland R. S., Wagner S. J., 2005, in Aharonian F., ed., What gamma rays tell us about jets. AIP, New York, p. 140
- Bicknell G. V., Saxton C. J., Sutherland R. S., 2003, Pub. Astron. Soc. Austral., 20, 102
- Blondin J. M., Lukfin E. A., 1993, ApJS, 88, 589
- Chatzichristou E. T., 2001, in Schilizzi R. T., ed., Proc. IAU Symp. 205, Galaxies and their Constituents at the Highest Angular Resolutions. Astron. Soc. Pac., San Francisco, p. 162
- Colella P., Woodward P. R., 1984, J. Comput. Phys., 54, 174
- Conway J. E., 2002a, New Astron. Rev., 46, 263
- de Vries W. H. et al., 1997, ApJS, 110, 191
- de Vries W. H., O’Dea C. P., Baum S. A., Barthel P. D., 1999, ApJ, 526, 27
- Drake C. L., McGregor P. J., Bicknell G. V., Dopita M. A., 2003, Pub. Astron. Soc. Austral., 20, 57
- Fragile P. C., Murray S. D., Anninos P., van Breugel W., 2004, ApJ, 604, 74
- Giovannini G., Cotton W., Feretti L., Lara L., Venturi T., 2000, Adv. Space Res., 26, 693
- Hardee P. E., Norman M. L., 1988, ApJ, 334, 70
- Kawakatu N., Umemura M., Mori M., 2003, ApJ, 583, L85
- Komissarov S. S., Falle S. A. E. G., 1996, in Hardee P. E., Bridle A. H., Zensus J. A., eds, Energy Transport in Radio Galaxies and Quasars. ASP Conf. Series. Astron. Soc. Pac., San Francisco, p. 173
- Labiano A. et al., 2003, Pub. Astron. Soc. Austral., 20, 28
- Lind K. R., Payne D. G., Meier D. L., Blandford R. D., 1989, ApJ, 344, 89
- Magorrian J. et al., 1998, AJ, 115, 2285
- Murgia M., 2003, Pub. Astron. Soc. Austral., 20, 19
- Murgia M., Fanti C., Fanti R., Gregorini L., Klein U., Mack K.-H., Vigotti M., 1999, A&A, 345, 769
- Murgia M., Fanti C., Fanti R., Gregorini L., Klein U., Mack K.-H., Vigotti M., 2002, New Astron. Rev., 46, 307
- O’Dea C. P. et al., 2002, AJ, 123, 2333
- O’Dea C. P. et al., 2003, Pub. Astron. Soc. Austral., 20, 88
- Owen F. N., Eilek J. A., Kassim N. E., 2000, ApJ, 543, 611
- Parma P., Murgia M., Morganti R., Capetti A., de Ruiter H. R., Fanti R., 1999, A&A, 344, 7
- Piner B. G., Unwin S. C., Wehrle A. E., Edwards P. G., Fey A. L., Kingham K. A., 1999, ApJ, 525, 176
- Rosen A., Hughes P. A., Duncan G. C., Hardee P. E., 1999, ApJ, 516, 729
- Saxton C. J., Sutherland R. S., Bicknell G. V., 2001, ApJ, 563, 103
- Saxton C. J., Sutherland R. S., Bicknell G. V., Blanchet G. F., Wagner S. J., 2002a, A&A, 393, 765
- Saxton C. J., Bicknell G. V., Sutherland R. S., 2002b, ApJ, 579, 176
- Silk J., Rees M. J., 1998, A&A, 331, L1
- Sutherland R. S., Bisset D. K., Bicknell G. V., 2003a, ApJS, 147, 187
- Sutherland R. S., Bicknell G. V., Dopita M. A., 2003b, ApJ, 591, 238
- Sutherland R. S., Dopita M. A., 1993, ApJS, 88, 253

Tremaine S. et al., 2002, ApJ, 574, 740

Van Breugel W. J. M., Filipenko A. V., Heckman T., Miley G. K., 1985, ApJ, 293, 83

Wiita P. J., Wang Z., Hooda J. S., 2002, New Astron. Rev., 46, 439

Wilkinson P. N., Tzioumis A. K., Benson J. M., Walker R. C., Simon R. S., Kahn F. D., 1991, Nat, 352, 313

## APPENDIX A: GRID SUBDIVISION FOR MULTIPROCESSOR COMPUTATION

We confront two practical obstacles to the calculation of high-resolution hydrodynamics simulations in higher dimensions: the duration of the run in real time (which inhibits the exploration of a wide parameter space), and the finite computer memory (which directly limits the number of grid cells that can be computed). We circumvent these limitations by subdividing the spatial grid into  $N = 2^n$  subgrids (with  $n$  an integer) and assigning each to a program running in parallel on a separate processor. The processors communicate between themselves using functions of the MPI (Message Passing Interface) library.<sup>2</sup>

If the global grid has dimensions of  $I \times J$  cells in the  $x$  and  $y$ -directions, then we define a ‘long subgrid’ as an area with  $I \times (J/N)$  cells (see the left-hand panel of Fig. A1), and a ‘wide subgrid’ as an area of  $(I/N) \times J$  cells (see the right-hand panel of Fig. A1). Within the memory at each processor we maintain representations of one long subgrid or one short subgrid: see for example the shaded long and wide subgrids held by processor 3 in Fig. A1. The total number of cells in a long subgrid is the same as that of a wide subgrid. In fact for each hydrodynamic variable on each processor, we identify the long and wide subgrid arrays with the same section of memory, which is feasible and reliable since the program uses only one of the subgrid representations at any time (as we shall detail below).

We then conceptually subdivide each long or wide subgrid into  $N$  blocks separated by transverse cuts (e.g. the dotted line divisions in the subgrids of processor 3 depicted in Fig. A1). For each processor  $p$  the block numbered  $p$  is the only area of overlap between the long and wide subgrids that it is assigned.

At the start of the simulation each processor is assigned long and wide subgrids according to its identity number. These regions are filled according to the initial conditions which are defined in terms of global grid coordinates. The first hydrodynamic sweep (Colella & Woodward 1984) is in the  $x$ -direction, and is performed by each processor within its long subgrid arrays (see left-hand panel of Fig. A2). Thus the  $x$ -sweeps do not encounter any of the subgrid interfaces, obviating the need for any communication of flux information between processors at this stage. The one-dimensional array vectors associated with each sweep are the maximum possible length, which makes optimal use of processor cache.

After the  $x$ -sweep is complete, the evolved density, velocity, pressure and other zone data are communicated between the processors. By use of the `MPL_ALLTOALL` function, the data of block  $i$  of the long subgrid of processor  $j$  is copied to block  $j$  of the wide subgrid of processor  $i$ , for all  $i$  and  $j$ . These are corresponding areas of the global computational grid. As the communication sequence proceeds, each processor receives data blocks and assembles them into complete, ordered arrays describing the wide subgrid that it is conceptually assigned. The wide subgrid arrays overwrite the memory areas that was previously used for long subgrid data. However the sequence

<sup>2</sup> <http://www-unix.mcs.anl.gov/mpl/>

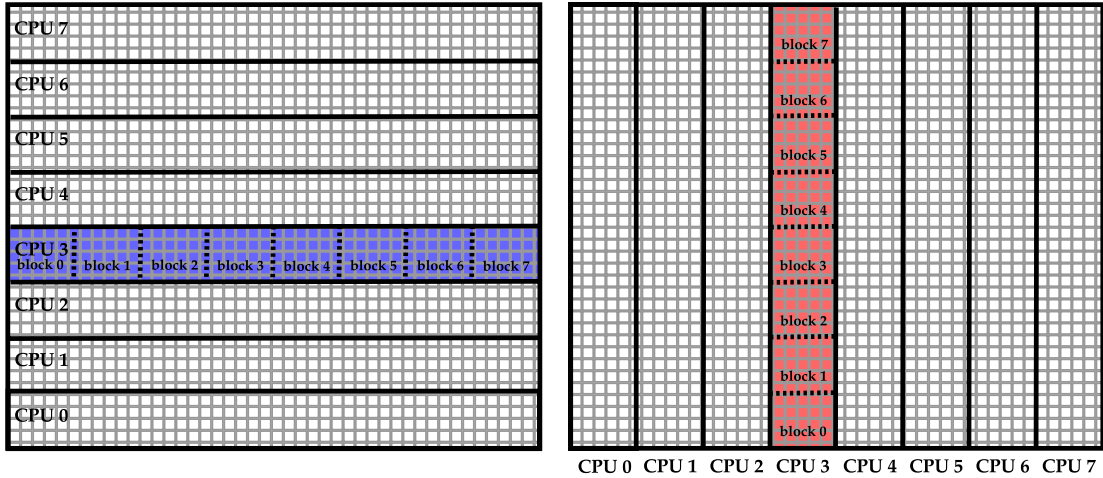


**Figure A1.** Distribution of the long and the wide subgrid partitions in a simulation run with eight processors. For illustrative clarification, the long subgrid assigned to processor 3 is highlighted in the left-hand panel, and the wide subgrid assigned to processor 3 is highlighted in the right-hand panel. The memory of each processor needs only to retain one long subgrid array and one wide subgrid array, plus scalar global variables. Collective maps of the global computational grid need only be assembled from output data files after the simulation is run.

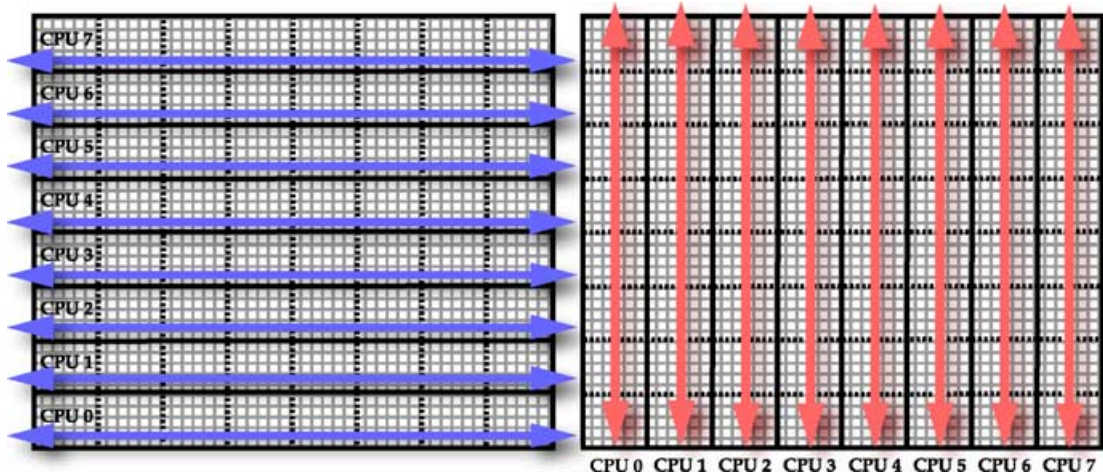


**Figure A2.** Hydrodynamic sweeps in the  $x$ -direction are only performed in the long subgrid arrays (left-hand panel), and sweeps in the  $y$ -direction are only performed in the wide subgrid arrays (right-hand panel). Thus every sweep operation occurs along the largest possible array dimension and involves only the arrays kept in the memory of the responsible processor. Communication between processors is required only to exchange updated block arrays of the hydrodynamic variables after each sweep is finished.

of the `MPI_ALLTOALL` communication provides for a complete redistribution of data across the set of processors without any collective loss of information.

When the communication is complete, each processor performs a hydrodynamic sweep in the  $y$ -direction within its respective wide subgrid arrays. (See right-hand panel of Fig. A2.) Again, as in the  $x$ -sweep, no processor boundaries are encountered during the computation, and the one-dimensional sweep arrays are long. At the end of the  $y$ -sweep, the processors communicate blocks of their evolved wide grid arrays in another `MPI_ALLTOALL` operation, ensuring that the long subgrid arrays are up to date. At this point program control operations are performed, e.g. generating output files recording the hydrodynamic variable arrays of each processor.

Care is needed to ensure that the processors evolve their subgrids synchronously in simulation time. Within each subgrid  $g$  the maximum allowable time-step of integration for each  $x$ - or  $y$ -sweep is

determined by a Courant condition:  $\delta t_g$  must be less than the characteristic time-scales of fluid motion or sound waves crossing a cell, e.g.  $\delta t_g < 0.6 \min(\delta x/v_{x,i}, \delta x/c_{s,i})$ , for all cells  $i$  with side-length  $\delta x$ . In order to synchronize the simulation across all the subgrids, the processors are made to intercommunicate their locally calculated values of  $\delta t_g$ , and then adopt the global minimum allowable time-step,  $\delta t = \min(\delta t_0, \delta t_1, \dots, \delta t_{N-1})$ .

This straightforward scheme for multiprocessor PPM hydrodynamics simulations is readily generalized to a three-dimensional grid. The 3D analogues of long and wide subgrids are ‘flat slabs’ (full size in the  $x$ - and  $y$ -directions, but subdivided into  $N$  segments in the  $z$ -direction) and ‘tall slabs’ (full size in the  $x$ - and  $z$ -directions, but subdivided into  $N$  parts in the  $y$ -direction). Using 32, 64, 128 or more of the processors of the Australian National University’s Compaq Alphaserver SC, we have been able to perform 3D simulations with cubic dimensions of 256, 512 or more cells per side (work in preparation).

## APPENDIX B: SELF-SIMILAR SOLUTION FOR INFLATION OF A TWO-DIMENSIONAL BUBBLE

### B1 Dimensional analysis

This appendix provides an analytical solution that can be used for the comparison of slab-jet simulations with expected asymptotic behaviour. The two parameters that determine the evolution of the bubble are  $A$ , the energy flux per unit transverse length, and  $\rho_0$  the density of the background medium. In terms of jet parameters,

$$A = \left( \frac{1}{2} \rho v^2 + \frac{\gamma}{\gamma - 1} p \right) v D \quad (\text{B1})$$

where  $D$  is the width of the jet.

Consider the parameter  $A/\rho_0$ . The dimensions of this parameter are given by:

$$\left[ \frac{A}{\rho_0} \right] = L^4 T^{-3} \Rightarrow \left[ \frac{A}{\rho_0} \right]^{1/4} = L T^{-3/4}. \quad (\text{B2})$$

Let  $R(t)$  be the bubble radius at time  $t$ . The dimensions of  $R t^{-3/4}$  are also  $L T^{-3/4}$ . Hence the self-similar evolution of the bubble will be given by:

$$\frac{R}{t^{3/4}} = C \left[ \frac{A}{\rho_0} \right]^{1/4} \quad (\text{B3})$$

where  $C$  is a numerical constant to be determined. The radius of the bubble is therefore given as a function of time by:

$$R = C \left[ \frac{A}{\rho_0} \right]^{1/4} t^{3/4}. \quad (\text{B4})$$

This derivation is justified and elaborated in the next section, where the constant  $C$  is derived.

### B2 Temporal evolution of bubble

#### B2.1 Formulation of equations

Consider a cylindrical bubble that is being fed by a jet with an energy density per unit length (transverse to the jet) equal to  $A$ . We consider the jet energy to be effectively thermalized so that the pressure derived from the shocked jet plasma drives cylindrical expansion. Let the energy density of the bubble be  $\epsilon$  and the pressure of the bubble be  $p$ .

We represent the bubble in two dimensions in the  $xy$ -plane and take a length,  $L$ , of bubble in the  $z$ -direction. The total energy,  $E = \epsilon \pi R^2 L$ , of this length of bubble with volume  $\pi R^2 L$  is governed by the equation:

$$\frac{d}{dt}(\epsilon \pi R^2 L) + p \frac{d}{dt}(\pi R^2 L) = A L. \quad (\text{B5})$$

The second term represents the work done by the pressure during the expansion; the term on the right represents the rate of energy fed into the bubble. Note that we are assuming that the dominant form of energy in this bubble is internal and that kinetic energy does not contribute significantly.

Taking out the common factor of  $L$ , the evolution of the bubble is governed by the equation

$$\frac{d}{dt}(\epsilon \pi R^2) + p \frac{d}{dt}(\pi R^2) = A. \quad (\text{B6})$$

We solve this equation by introducing the equation of state,  $\epsilon = p/(\gamma - 1)$ , and by relating the pressure in the bubble to its rate of expansion.

Assuming that the bubble is expanding supersonically with respect to the background medium, then its structure consists of a strong shock outside the bubble and a contact discontinuity separating the bubble material from the shocked ISM. In this region, the pressure of the shocked ISM and the bubble are equal. Suppose that the strong shock is moving with velocity  $v_{\text{sh}}$ . Then the gas behind the shock is moving with speed  $3v_{\text{sh}}/4$  so that

$$\dot{R} = \frac{3}{4} v_{\text{sh}}. \quad (\text{B7})$$

Let the density of the background medium be  $\rho_0$ . Then the pressure behind the shock is given by

$$p \approx \frac{3}{4} \rho_0 v_{\text{sh}}^2 \approx \frac{4}{3} \rho_0 \dot{R}^2. \quad (\text{B8})$$

Note that we have not specified the  $\gamma$  for the bubble but we have assumed that  $\gamma = 5/3$  for the background ISM.

Substituting the equation of state into (B6), and expanding the first term, the bubble equation becomes:

$$\frac{\gamma}{\gamma - 1} \pi p \frac{dR^2}{dt} + \frac{1}{\gamma - 1} \pi R^2 \frac{dp}{dt} = A. \quad (\text{B9})$$

Then, using equation (B8) for the pressure, we obtain, after some simplification:

$$R \dot{R}^3 + \frac{1}{\gamma} R^2 \dot{R} \ddot{R} = \frac{\gamma - 1}{\gamma} \frac{3A}{8\pi\rho_0}. \quad (\text{B10})$$

#### B2.2 Solution

It would be reasonably straightforward to develop a general solution of equation (B10). However, we settle for a self-similar solution, for which:

$$R = a t^\alpha \quad (\text{B11})$$

where  $a$  and  $\alpha$  are constants. Substitution into equation (B10) gives:

$$a^4 \alpha^2 \left[ \alpha + \frac{\alpha - 1}{\gamma} \right] t^{4\alpha - 3} = \frac{\gamma - 1}{\gamma} \frac{3A}{8\pi\rho_0}. \quad (\text{B12})$$

Equating the powers of  $t$  on both sides:

$$\alpha = \frac{3}{4} \quad (\text{B13})$$

as expected. Equating the constants:

$$a = \left[ \frac{3}{8} \frac{\gamma - 1}{\alpha^2 [(\gamma + 1)\alpha - 1]} \frac{A}{\pi\rho_0} \right]^{1/4}. \quad (\text{B14})$$

The form of the dependence on the parameter  $A/\rho_0$  was anticipated in Section B1. For  $\gamma = 5/3$ , as used in our simulations:

$$a = \left[ \frac{4A}{9\pi\rho_0} \right]^{1/4} \quad (\text{B15})$$

and the solution for  $R$  is:

$$R = \left[ \frac{4A}{9\pi\rho_0} \right]^{1/4} t^{3/4}. \quad (\text{B16})$$

**B3 Radius of shock wave**

In comparing the analytic solution with simulations it is easiest to locate the position of the discontinuity in the pressure. This is the location of the outer shock wave, whose velocity is derived from equation (B7), i.e.

$$v_{\text{sh}} = \frac{4}{3} \dot{R}. \quad (\text{B17})$$

Hence the radius of the pressure discontinuity is given by

$$R_{\text{p}} = \frac{4}{3} a t^{\alpha} = \frac{4}{3} \left[ \frac{4A}{9\pi\rho_0} \right]^{1/4} t^{3/4} \quad (\text{B18})$$

for  $\gamma = 5/3$ .

This paper has been typeset from a  $\text{\TeX}/\text{\LaTeX}$  file prepared by the author.